Journal of the Meteorological Society of Japan, Vol. 93, No. 1, pp. 5−48, 2015
DOI:10.2151/jmsj.2015-001

The JRA-55 Reanalysis: General Specifications and Basic Characteristics

Shinya KOBAYASHI, Yukinari OTA, Yayoi HARADA

Japan Meteorological Agency, Tokyo, Japan
Meteorological Research Institute, JMA, Tsukuba, Japan

Ayataka EBITA

Meteorological Research Institute, JMA, Tsukuba, Japan

Masami MORIYA, Hirokatsu ONODA, Kazutoshi ONOGI

Japan Meteorological Agency, Tokyo, Japan

Hirotaka KAMAHORI, Chiaki KOBAYASHI, Hirokazu ENDO

Meteorological Research Institute, JMA, Tsukuba, Japan

Kengo MIYAOKA and Kiyotoshi TAKAHASHI

Japan Meteorological Agency, Tokyo, Japan

(Manuscript received 13 March 2014, in final form 18 September 2014)

Abstract

The Japan Meteorological Agency (JMA) conducted the second Japanese global atmospheric reanalysis, called the Japanese 55-year Reanalysis or JRA-55. It covers the period from 1958, when regular radiosonde observations began on a global basis. JRA-55 is the first comprehensive reanalysis that has covered the last half-century since the European Centre for Medium-Range Weather Forecasts 45-year Reanalysis (ERA-40), and is the first one to apply four-dimensional variational analysis to this period. The main objectives of JRA-55 were to address issues found in previous reanalyses and to produce a comprehensive atmospheric dataset suitable for studying multidecadal variability and climate change. This paper describes the observations, data assimilation system, and forecast model used to produce JRA-55 as well as the basic characteristics of the JRA-55 product.

JRA-55 has been produced with the TL319 version of JMA's operational data assimilation system as of December 2009, which was extensively improved since the Japanese 25-year Reanalysis (JRA-25). It also uses several newly available and improved past observations. The resulting reanalysis products are considerably better than the JRA-25 product. Two major problems of JRA-25 were a cold bias in the lower stratosphere, which has been diminished, and a dry bias in the Amazon basin, which has been mitigated. The temporal consistency of temperature analysis has also been considerably improved compared to previous reanalysis products. Our initial quality evaluation revealed problems such as a warm bias in the upper troposphere, large upward imbalance in the global mean net energy fluxes at the top of the atmosphere and at the surface, excessive precipitation over the tropics, and unrealistic trends in analyzed tropical cyclone strength. This paper also assesses the impacts of model biases and changes in the observing system, and mentions efforts to further investigate the representation of low-frequency variability and trends in JRA-55.

Keywords reanalysis; data assimilation; meteorological observation; numerical weather prediction

Corresponding author: Shinya Kobayashi, Japan Meteorological Agency, 1-3-4, Ote-machi, Chiyoda-ku, Tokyo 100-8122, Japan
E-mail: s-kobayashi@met.kishou.go.jp

1. Introduction

Reanalysis of past observations with a consistent, state-of-the-art data assimilation system aims at producing a high-quality climate dataset. It can

produce a dataset for numerous types of meteorological variables, including those for which observations are sparse, in a physically consistent, spatiotemporally regular manner. Reanalyses have been widely used for research into the mechanisms of the earth's climate system, the study of predictability, and climate monitoring. Reanalysis has made significant contributions to research on synoptic and planetary scale phenomena such as storm tracks, blocking, the Madden-Julian oscillation, the El Ninõ/Southern Oscillation and quasi-biennial oscillation, and verification of the reproducibility of these phenomena in forecast models. Continued improvement of reanalyses is crucial to advance climate research and improve climate services.

Reanalysis efforts are continually undertaken at major numerical weather prediction (NWP) centers and meteorological research institutes (a detailed list is available at http://www.reanalyses.org). The quality of recent reanalyses has markedly improved because of progress in rescuing and homogenizing past observations and advances in data assimilation techniques. In Japan, the Japanese 25-year Reanalysis (JRA-25) was jointly conducted by the Japan Meteorological Agency (JMA) and the Central Research Institute of Electric Power Industry (CRIEPI) (Onogi et al. 2007). Its representation of precipitation distribution, tropical cyclones, and stratocumulus along the western coast of continents was the best available at that time. However, it suffered from problems such as a cold bias in the lower stratosphere and a dry bias in the Amazon basin. Its reanalysis period, which went back only to 1979, was not long enough for the studies of multidecadal variability and climate change. It also shared problems that are general to reanalysis, including quality changes that arise from changes of observing systems and the reproducibility of fluxes between climate subsystems such as atmosphere–ocean and atmosphere–land fluxes (Bengtsson et al. 2007).

Since the JRA-25 data assimilation system has been built, JMA's operational NWP system has improved in many aspects, including revision of the longwave radiation scheme and introduction of four-dimensional variational analysis (4D-Var) and variational bias correction (VarBC) for satellite radiances. These improvements have significantly reduced model biases, improved the dynamical consistency of analysis fields, and advanced handling of satellite radiances. Ongoing efforts to improve the quality of past observations include homogenization of radiosonde temperature observations (Haimberger et al. 2008, 2012) and reprocessing of observations at major meteorological satellite centers.

Taking advantage of these improvements, JMA has conducted the second Japanese global atmospheric reanalysis, called JRA-55. As mentioned in the interim report (Ebita et al. 2011), the data cover the period starting from 1958 when regular radiosonde observations began on a global basis. JRA-55 is the first comprehensive reanalysis to cover the last half-century since the European Centre for Medium-Range Weather Forecasts 45-year Reanalysis (ERA-40, Uppala et al. 2005) and the first to apply 4D-Var to this period. Its main objectives were to address the issues identified in previous reanalyses and to produce a comprehensive atmospheric dataset suitable for the studies of multidecadal variability and climate change.

As the comprehensive report on JRA-55, this paper outlines the general specifications and basic characteristics of JRA-55. Data sources, quality control (QC), and data selection for observations are explained in Section 2. The data assimilation system and the forecast model are described in Sections 3 and 4, respectively. Computational environment and production streams are summarized in Section 5. Section 6 examines the basic performance of the data assimilation system with fits to observation, analysis increments, and forecast scores. Section 7 focuses on two major improvements in quality over the JRA-25 product, the temporal consistency of the temperature analysis, and the representation of the South American monsoon system. Section 8 reviews the basic characteristics of the products. Conclusions are presented in Section 9. Appendix B contains a list of the acronyms used in this paper.

2. Observations

2.1 Data sources

Observations used in JRA-55 primarily consist of those used in ERA-40 (Uppala et al. 2005) and those archived by JMA. The ERA-40 observational dataset was supplied to JMA by the European Centre for Medium-Range Weather Forecast (ECMWF) for use in the JRA-25 project (Onogi et al. 2007). Observations for the period starting in 1979 are basically the same ones used in JRA-25. In addition, newly available observational datasets were collected and used whenever possible. A detailed list of data suppliers and the type of data provided by them is given in appendix A.

Reports of surface observation from fixed land stations (SYNOP) and upper-level observations used

in the National Centers for Environmental Prediction (NCEP)/National Center for Atmospheric Research (NCAR) reanalysis (Kalnay et al. 1996; Kistler et al. 2001) were used on a supplementary basis for the year 1979 because those observations were incomplete in the ERA-40 observational dataset. Wind profile retrievals surrounding tropical cyclones (TCRs) (Fiorino 2002) were regenerated with improved QC for best-track data and supplied by Dr. Michael Fiorino.

Snow depths from Russia, the USA, and Mongolia were provided by the Russian Research Institute for Hydrometeorological Information (RIHMI), the University Corporation for Atmospheric Research (UCAR) (NCDC et al. 1981), and the Institute of Meteorology and Hydrology (IMH), respectively. These datasets were used in preference to the operational archives in the snow depth analysis component because they have fewer gaps and contain fewer errors due to miscoded reports from the Global Telecommunication System.

Recently, major meteorological satellite centers have been reprocessing historical satellite observations with the latest algorithms to produce high-quality, homogeneous satellite products. The JMA Meteorological Satellite Center (MSC) reprocessed atmospheric motion vectors (AMVs) and clear sky radiances (CSRs) from past Geostationary Meteorological Satellite (GMS) and Multi-functional Transport Satellite (MTSAT) imagery with the latest derivation algorithms as of 2009, which was a pilot project in the Sustained, Coordinated Processing of Environmental Satellite Data for Climate Monitoring (SCOPE-CM) initiative (http://www.wmo.int/pages/prog/sat/scope-cm_en.php). JRA-55 is the first reanalysis to assimilate the newly reprocessed AMVs and CSRs from these satellites.

2.2 *Quality control and data selection*

Observational datasets contain poor-quality data resulting from instrument malfunctions, human errors, and inadequate metadata. These kinds of poor-quality data must be identified and excluded before the assimilation step. It is common practice to automatically exclude observations that are inconsistent with others or outliers from background fields (JMA 2007; Onogi et al. 2007). Offline QC is also an effective measure for reanalysis because analysis of a past period is free from constraints of a real-time operation. In addition to poor-quality data, observations unsuitable for assimilation are excluded, such as those that are far less accurate than background, those whose spatial representativeness considerably differs from that of background, or for which background equivalents cannot be generated with sufficient accuracy.

The following subsections explain the QC and data selection methods used for each observation type in JRA-55.

a. Conventional data

The QC procedure for conventional data was basically the same as the one used for JRA-25, including a climatological check, track check, consistency check, gross error check, etc (Onogi et al. 2007). A notable feature of the QC methods used in JMA's data assimilation system is "Dynamic QC," in which the threshold value is defined as a variable linearly depending on the local horizontal gradient and tendency of the first-guess fields (Onogi 1998). Since JRA-25, the set of QC thresholds has been thoroughly reviewed and updated (Sakamoto 2009).

Another important QC task was the removal of duplicates. Because the observational dataset used for JRA-55 had multiple data sources, there were many duplicates. However, it is difficult to identify and completely remove duplicates because metadata (such as location, time and level) did not always match among different data sources. To minimize duplications, the ERA-40 observational dataset was preferred over others in most cases because it is the most consolidated observational dataset among those used for JRA-55.

TCRs are assimilated with the same prescribed observational errors as those used for typhoon bogus data in JMA's operational system. The data consist of 6-hourly winds on standard pressure levels from 1000 hPa to 400 hPa at the centers of tropical cyclones and at 2° latitude/longitude away from those points in the four cardinal directions.

Table 1 compares data counts, rejection rates, and utilization rates for each type of conventional observation used in JRA-55 with those used in JRA-25 for the year 1995; Table 2 does the same with those used in JMA's operational system for the year 2010. Data excluded by blacklisting or preliminary screening are not included in the statistics.

The number of observations ingested in JRA-55 is smaller than that in JRA-25 for 1995 because JRA-55 ingested conventional observations from JMA's archive before August 2002 only over Japan, whereas JRA-25 ingested all available observations. Another notable difference between JRA-25 and JRA-55 is the greater rejection rates of upper-level observations due to the tightening of QC thresholds in JRA-55.

Table 1. Data counts and QC statistics for conventional data in JRA-25 and JRA-55 for the year 1995.

Obs type	Parameter	Level	Ingested obs		Rejected obs (%)		Used obs (%)	
			JRA-25	JRA-55	JRA-25	JRA-55	JRA-25	JRA-55
SYNOP	*P*	surface	14445140	10615854	2.16	3.22	36.11	42.34
SHIP	*P*	surface	2524820	2391174	3.38	7.85	44.36	43.18
BUOY	*P*	surface	2697799	2048419	2.12	5.55	8.65	10.45
Upper-level	*T*	~100 hPa	5055575	4409306	0.96	6.03	42.31	44.60
Upper-level	*T*	100~1000 hPa	12265485	10642362	0.63	5.90	38.54	41.78
Upper-level	*u*	~100 hPa	4884545	3953650	0.85	1.76	42.33	47.56
Upper-level	*u*	100~1000 hPa	12143438	8853872	0.49	3.11	44.62	55.45
Upper-level	*Rh*	100~1000 hPa	10985799	9109329	0.01	1.03	27.91	31.90
Aircraft	*u*	100~1000 hPa	14082016	6664082	1.45	3.80	14.44	27.99
Profiler (US)	*u*	100~1000 hPa	8051614	7835794	3.95	4.09	4.16	4.26

Table 2. Data counts and QC statistics for conventional data in JMA's operational system and JRA-55 for the year 2010.

Obs type	Parameter	Level	Ingested obs		Rejected obs (%)		Used obs (%)	
			Oper	JRA-55	Oper	JRA-55	Oper	JRA-55
SYNOP	*P*	surface	19181647	18701759	2.01	2.17	30.51	29.79
SHIP	*P*	surface	1152820	1173037	2.70	3.36	35.73	35.53
BUOY	*P*	surface	7040018	7296503	0.93	1.19	14.80	14.69
Upper-level	*T*	~100 hPa	6631550	6952966	3.92	3.68	39.66	38.12
Upper-level	*T*	100~1000 hPa	13696594	14399844	3.97	3.99	36.07	34.34
Upper-level	*u*	~100 hPa	8808256	8953899	1.45	1.37	28.73	28.31
Upper-level	*u*	100~1000 hPa	13192314	13377604	1.99	2.13	37.67	37.10
Upper-level	*Rh*	100~1000 hPa	12451435	12963016	0.93	0.88	26.38	25.27
Aircraft	*u*	100~1000 hPa	34745677	75256027	0.93	1.18	17.72	11.00
Profiler (US)	*u*	100~1000 hPa	7469265	7468709	5.07	5.04	4.24	4.30
Profiler (Japan)	*u*	100~1000 hPa	22695916	22696592	6.78	7.32	0.80	0.79
Profiler (Europe)	*u*	100~1000 hPa	13695644	13702435	9.30	9.63	0.94	0.95

Unlike operational systems, reanalysis has no constraint of cutoff time. Thus, JRA-55 ingested more observations than JMA's operational system for the year 2010, except for surface pressure observations from SYNOP. In JRA-55, surface pressure observations over the Amazon basin were entirely excluded because of their inconsistency with background fields. Further detail is given in Section 7.2.

JRA-55 ingested twice as many aircraft observations as JMA's operational system. Aircraft observations over the continental United States were thinned to one-fiftieth by preliminary screening in the operational system (JMA 2013b, Section 2.2.2.7), whereas no preliminary screening was performed for JRA-55 because coverage of earlier aircraft observations is too sparse to apply this screening. In JMA's operational system, temperature data from aircraft are used with bias corrections that are estimated using one-month statistics for each aircraft identifier (Sako 2010). However, because many of the older aircraft observations had unknown identifiers, this bias correction method could not be used for the reanalysis. Therefore, temperatures from aircraft are not used in JRA-55.

Radiosonde temperature records contain numerous discontinuities arising from factors such as modifications in radiosonde instrument. In particular, numerous radiosonde temperature observations before the 1980s had a significant warm bias mainly caused by radiation effects (Onogi 2000). It is crucial to remove these biases before using these records for climate applications.

JRA-25 used the method of Andræ et al. (2004) to correct temperature bias. Their method uses statistics for each country or region under the assumption that each uses a similar type of radiosonde to calculate the bias for four classes of solar elevation. The coefficients are recalculated every month by the departure

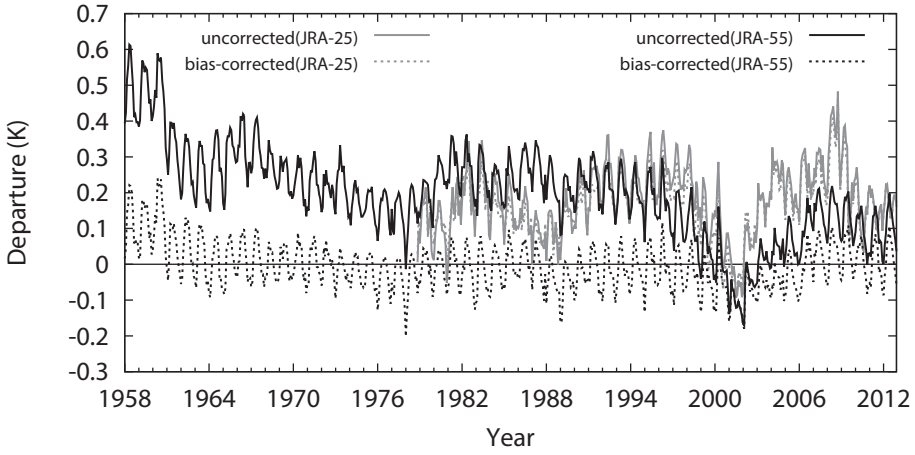

Fig. 1. Monthly mean background departures for temperature observations from radiosondes at levels near 300 hPa averaged over the extratropical northern hemisphere from JRA-25 and JRA-55. Uncorrected background departures are shown in solid lines and bias-corrected departures in dotted lines.

statistics of the latest 12 months (Onogi et al. 2007).

JRA-55 performed bias correction for radiosonde temperature using the Radiosonde Observation Correction using Reanalysis (RAOBCORE) version 1.4 (Haimberger et al. 2008) until the end of 2006, and RAOBCORE version 1.5 (Haimberger et al. 2012) thereafter. Bias estimates were produced for each station by applying a statistical break detection method to the departure values from ERA-40 and ERA-Interim (Dee et al. 2011). Because bias estimates for the hours of 06 and 18 UTC are not available in RAOBCORE, bias estimates for either 00 or 12 UTC were substituted assuming that biases did not significantly vary within the daytime and nighttime hours.

Figure 1 shows time series from JRA-25 and JRA-55 for monthly mean background departures (observations minus background) for temperature observations from radiosondes at levels near 300 hPa, averaged over the extratropical northern hemisphere. The uncorrected departures exhibit larger warm biases in early years. These were significantly reduced by RAOBCORE in JRA-55, whereas differences between the uncorrected and bias-corrected departures in JRA-25 are very small, indicating a small impact of the bias correction. The bias-corrected time series from JRA-55 exhibits seasonal variations because dependencies of biases on solar elevations were not taken into account.

b. Satellite radiances

(1) Infrared sounders

Because JRA-55 does not simulate the effects of clouds on satellite radiances, cloud-contaminated observations are identified and rejected before the assimilation step. Whereas JRA-25 performed cloud detection using window channels (Sakamoto and Christy 2009), JRA-55 uses an improved cloud detection scheme based on Krzeminski et al. (2009).

Table 3 summarizes the Vertical Temperature Profile Radiometer (VTPR) and the High-Resolution Infrared Spectrometer (HIRS) observations used in JRA-55 (the available period for each type of observation is given in appendix A). While stratospheric temperature channels, of which the central wavenumber is located near 680 cm^{-1}, are not subject to cloud detection, tropospheric temperature, and humidity channels are only used in clear sky condition. Channels sensitive to the ground are excluded over land and sea ice because surface temperature and emissivity estimates over those regions are not very reliable. All the observations over the Caspian Sea are excluded for the same reason. In addition, observations near both the ends of scan lines are excluded because they tend to exhibit large biases because of various reasons such as incomplete radiative transfer modeling at large viewing angles.

For the Stratospheric Sounding Unit (SSU), observations from all the channels are assimilated.

Table 3. VTPR and HIRS/2 observations used in JRA-55. Central wavenumbers are from McMillin et al. (1973) for VTPR and Werbowetzki (1981) for HIRS/2.

Channel	Central wavenumber (cm^{-1})	Land or sea ice		Sea	
		Cloudy	Clear	Cloudy	Clear
VTPR					
1	668.5				
2	677.5	○	○	○	○
3	695.0		○		○
4	708.0				○
5	725.0				○
6	747.0				○
7	535.0		1500 m*		○
8	833.0				

*Not used if the surface height is greater than the given value.
Note: Observations from the fields of view (FOVs) 1 and 23, which are located at both ends of scan lines, and all observations over the Caspian Sea are excluded.

HIRS/2					
1	669				
2	680	○	○	○	○
3	690		○		○
4	703				○
5	716				○
6	733				○
7	749				○
8	900				
9	1030				
10	1225				
11	1365				○
12	1488		1500 m*		○
13	2190				
14	2210				○
15	2240				○
16	2270				
17	2360				
18	2515				
19	2660				
20	14500				

*Not used if the surface height is greater than the given value.
Note: Observations from the FOVs 1–3 and 54–56, which are located at both ends of scan lines, and all observations over the Caspian Sea are excluded.

(2) Microwave sounders

Table 4 summarizes microwave sounder observations used in JRA-55. In the microwave region, wavelengths are far larger than the size of water droplets and ice crystals; hence, absorption and scattering by those particulates is mostly negligible, except in the presence of raindrops. In JRA-25, however, cloud detection for the Microwave Sounding Unit (MSU) was performed using the scheme for HIRS, the infrared sounder on the same satellite; consequently, some usable tropospheric observations were rejected. In JRA-55, cloud detection for MSU uses first-guess departures of the window channel (channel 1) of its own instrument to retain as many observations as possible.

Cloud and rain detection for the Advanced Microwave Sounding Unit (AMSU)-A is performed using a

Table 4. Microwave sounder observations used in JRA-55. Frequencies are from Werbowetzki (1981) for MSU and Robel (2009) for AMSU-A, AMSU-B, and MHS.

Channel	Frequency (GHz)	Land or sea ice		Sea		
		Rainy/ Cloudy	Clear	Rainy	Cloudy	Clear
MSU						
1	50.3					
2	53.74					○
3	54.96			○	○	○
4	57.95	○	○	○	○	○
Note: Observations from the FOVs 1 and 11, which are located at both ends of scan lines, are excluded.						
AMSU-A						
1	23.800					
2	31.400					
3	50.300					
4	52.800					○
5	53.596 ± 0.115					○
6	54.400		1500 m*			○
7	54.940		2500 m*		○	○
8	55.500		○		○	○
9	f_0 = 57.290344	○	○	○	○	○
10	f_0 ± 0.217	○	○	○	○	○
11	f_0 ± 0.3222 ± 0.048	○	○	○	○	○
12	f_0 ± 0.3222 ± 0.022	○	○	○	○	○
13	f_0 ± 0.3222 ± 0.010	○	○	○	○	○
14	f_0 ± 0.3222 ± 0.0045	○	○	○	○	○
15	89.000					
*Not used if the surface height is greater than the given value.						
AMSU-B/MHS						
1	89.0 ± 0.9/89.0					
2	150.0 ± 0.9/157.0					
3	183.31 ± 1.00/183.311 ± 1.0				○	○
4	183.31 ± 3.00/183.311 ± 3.0				○	○
5	183.31 ± 7.00/190.311				○	○

scattering index for all surface types as well as total column cloud water retrievals over sea. The total column cloud water retrievals are computed with the algorithm that has been updated since JRA-25 (Okamoto et al. 2007). AMSU-A radiances are considered to be contaminated by clouds if the total column cloud water retrieval exceeds 100 g m^{-2} and by rain if the value exceeds 300 g m^{-2}.

For AMSU-B and the Microwave Humidity Sounder (MHS), radiances satisfying the following criterion are considered to be contaminated by rain;

$$T_b\,(\mathrm{ch1}) - T_b\,(\mathrm{ch2}) > 3\ \mathrm{K}$$

where T_b is the observed brightness temperature. This criterion was derived from the fact that T_b (ch1) is colder than T_b (ch2) in clear sky condition due to the effect of water vapor continuum absorption.

(3) Microwave imagers

In JRA-25, precipitable water contents were first retrieved from microwave imager radiances with the algorithm of Takeuchi (2002) and then assimilated in the atmospheric analysis component. In JRA-55, radiances from vertically polarized channels of four frequency bands around 19, 22, 37, and 90 GHz are directly assimilated over the sea after removing radi-

ances contaminated by thick clouds or rain.

Microwave imagers also make observations with horizontally polarized channels in the same frequency bands. These different polarized channels have the same atmospheric transmittances but different surface emissivities, which enables the retrieval of surface variables. In the atmospheric analysis component of JRA-55, however, radiances from horizontally polarized channels are not assimilated because satellite radiances have no direct influence on surface variables in the JRA-55 data assimilation system, except through the linearized model operator (Okamoto et al. 2008, 2011).

In the snow depth analysis component, daily snow cover retrievals from the Special Sensor Microwave/Imager (SSM/I) and the Special Sensor Microwave Imager Sounder (SSMIS) are used.

(4) CSRs

Radiances from water vapor channels of geostationary satellite imagers are assimilated in JRA-55 (Ishibashi 2009). While some recent geostationary satellites are equipped with multiple water vapor channels with differing weighting function peaks, e.g., the Spinning Enhanced Visible and Infrared Imager (SEVIRI) 6.2 and 7.3 μm channels on the Meteosat Second Generation (MSG) satellites, only the channel sensitive to the upper troposphere is used in JRA-55. This is because the surface emissivity over land is fixed at 0.9, and the radiance simulation for channels sensitive to the surface is not sufficiently accurate.

For the water vapor channel of GMS-5, the radiance simulation uses a corrected spectral response function proposed by Bréon et al. (1999).

c. AMVs

AMVs from geostationary and polar orbiting satellites have been used since January 1979 and June 2004, respectively. Reprocessed AMVs are used whenever available (Appendix A); otherwise operational AMVs are used. A QC procedure similar to the one described for conventional data is used for AMVs. In addition, data selection is performed using the AMV blacklist, which specifies the regions and levels for each type of sensor where AMVs are to be used. The quality indicators of Holmlund (1998) are also used for data selection if available (JMA 2013b).

For most operational AMVs prior to 1995, information on computation method, i.e., from which channel the wind is derived, is missing or encoded incorrectly. Data selection for those AMVs was performed as if they were from infrared channels.

d. Scatterometer ocean surface winds

The QC procedure for scatterometer ocean surface winds consists of the removal of ambiguity in wind direction, a gross error check, and "Group QC" (Ohhashi 2004), which restores winds rejected by the gross error check if they are spatially consistent (JMA 2013b). Background departures are computed using 10 m wind forecasts and then used as the departures for the lowest model level in the atmospheric analysis component.

Because winds from the Advanced Scatterometer (ASCAT) have a slow bias relative to the forecast model in strong winds, winds stronger than 15 m s^{-1} are not used. This criterion was also applied to reprocessed winds from the Active Microwave Instrument (AMI) (De Chiara et al. 2007), which were retrieved with the same model function used for ASCAT, the C-band model function (CMOD) 5.N (Hersbach 2008). For reprocessed winds from SeaWinds (Dunbar et al. 2006), data flagged as being in rain areas are not used (Ohhashi 2004).

Scatterometer ocean surface winds are also assimilated in the screen-level analysis component.

e. Global Navigation Satellite System–Radio Occultation (GNSS-RO) refractivities

The GNSS-RO refractivities have been used since July 2006 in JRA-55 but they were not used in JRA-25. The GNSS-RO observations can be assimilated without bias correction because they are derived from atmospheric time delays of radio signals, which can be measured by an atomic clock with high accuracy. The quality of GNSS-RO observations is hardly affected by surface and weather conditions. JRA-55 assimilates an average of approximately 500 refractivity profiles from the entire globe in every analysis cycle. Therefore, GNSS-RO observations together with radiosonde observations are important for constraining model biases and anchoring VarBC.

Because refractivity is a function of temperature, humidity, and pressure, it can be used to determine the profiles of these properties. Refractivity data for altitudes up to 30 km are used with 500-m vertical intervals. The assimilation of refractivity data is performed with a local operator, which only considers temperature, humidity, and pressure at the ray tangent point. The observation errors are defined as a function of height (JMA 2013b).

2.3 Coverage

Figure 2 shows the monthly mean counts of conventional upper-level observations, surface pres-

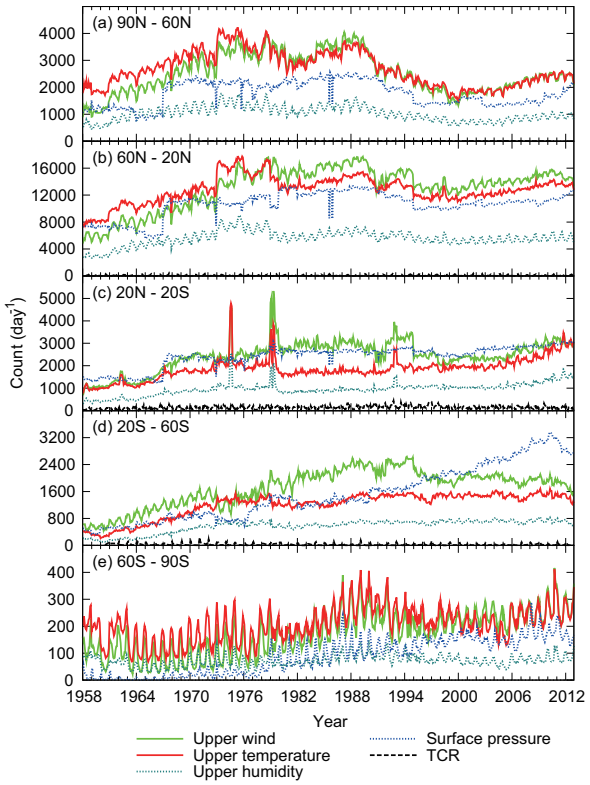

Fig. 2. Monthly mean counts of conventional upper-level observations, surface pressures, and TCRs assimilated in the atmospheric analysis component of JRA-55 in five latitude bands.

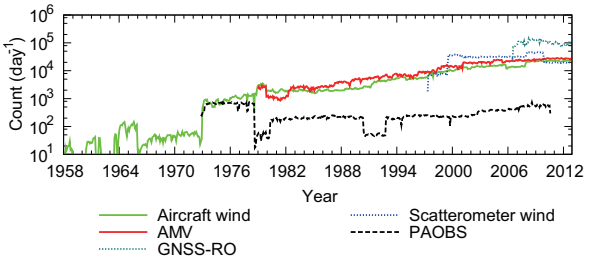

Fig. 3. Global monthly mean counts of aircraft and satellite winds, PAOBS, and GNSS-RO refractivities assimilated in the atmospheric analysis component of JRA-55.

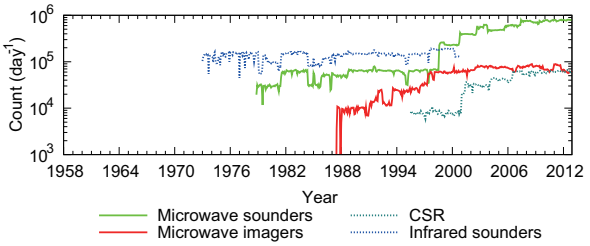

Fig. 4. Global monthly mean counts of various types of satellite radiances assimilated in the atmospheric analysis component of JRA-55.

sures, and TCRs assimilated in the atmospheric analysis component of JRA-55 in five latitude bands. The number of upper-level observations reached a peak in the late 1980s and then began to decline. A marked decline in the Arctic region was most likely because of station closures and cutbacks in the former Soviet Union. Observation counts picked up in the 2000s for reasons that may include increasing reports of significant levels, a rise in maximum altitudes, and decreasing rejection rates following the improvement in observation quality.

For surface pressure observations, there is a striking change in observation counts after 1967 in the northern hemisphere and tropics (Figs. 2a, b, c). Observation counts in 1965 and 1966 dipped sharply due to the lack of surface observations in Canada, Mexico, China, Mongolia, India, and most of Europe. On the other hand, observation counts in southern hemisphere mid-latitudes increased steadily (Fig. 2d).

The tropical record (Fig. 2c) shows occasional spikes in observation counts, as in 1979 when the First Global Experiment of the Global Atmospheric Research Programme (FGGE) was held. In the Antarctic region, observation counts show large seasonal increases in summer (Fig. 2e).

Figures 3 and 4 show global monthly mean counts of aircraft and satellite observations assimilated in the atmospheric analysis component of JRA-55. These types of observation first became available in significant numbers in 1973, and they have rapidly increased after the 1990s. Observation counts from infrared and microwave sounders on polar orbiting satellites dipped sharply in the 1980s when only a single polar orbiting satellite was operational.

For AMVs from geostationary satellites, observations first became available from all longitudes in 1979 when FGGE was held. Then, only GMS and the Geostationary Operational Environmental Satellite (GOES) continued observation until Meteosat-2 became operational in the early 1980s. Observations covered all longitudes again in 1998 when Meteosat-5 began observations over the Indian Ocean.

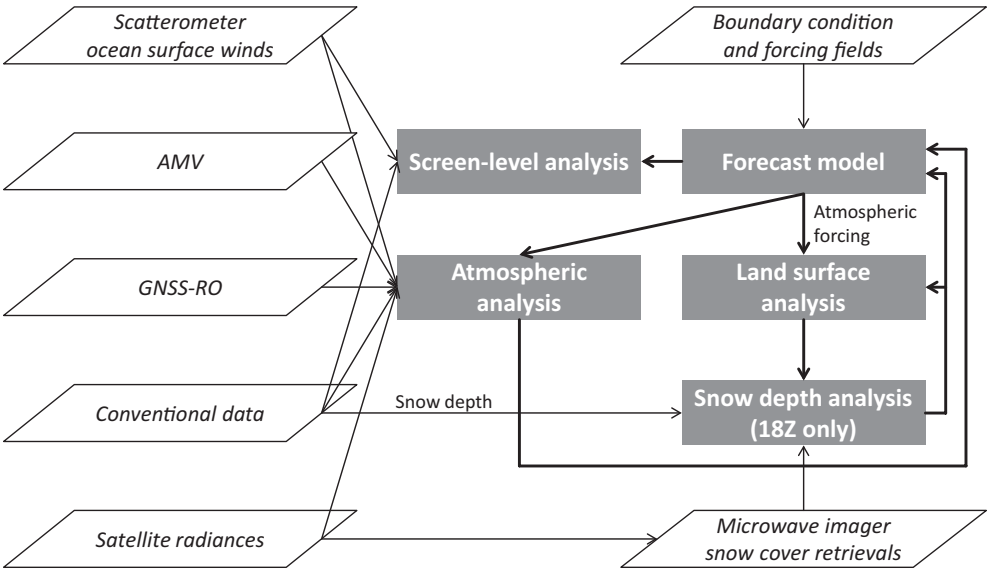

Fig. 5. Schematic of the main components of the JRA-55 data assimilation system and the data flow among them.

3. Data assimilation system

Figure 5 illustrates the main components of the JRA-55 data assimilation system and the data flow between them. Atmospheric analysis, screen-level analysis, and land surface analysis are performed at 00, 06, 12, and 18 UTC, and the snow depth analysis is performed at 18 UTC every day. The forecast model uses the most recent previous analysis as initial conditions, thereby generating background and atmospheric forcing fields that are necessary for analysis. Using these fields and observations, analysis fields are then generated as the most plausible state of the atmosphere. The JRA-55 system is based on the low-resolution (TL319) version of JMA's operational data assimilation system as of December 2009 (JMA 2007, 2013b), which has been improved extensively since JRA-25 (Table 5). Details of the products from the JRA-55 system are given in JMA (2013a, 2014).

3.1 Atmospheric analysis

The atmospheric analysis component of JRA-55 is based on incremental 4D-Var (Courtier et al. 1994). The analysis $\mathbf{z}^{\mathrm{a}} = \mathbf{z}^{\mathrm{b}} + \mathbf{\Delta z}$ is obtained through estimating the analysis increment $\Delta\mathbf{z}$ that minimizes the cost function J given by

$$J(\mathbf{\Delta z}_0) = \frac{1}{2}\mathbf{\Delta z}_0^{\mathrm{T}}\mathbf{B}^{-1}\mathbf{\Delta z}_0 + \frac{1}{2}\sum_{i=0}^{n}(\mathbf{H}_i\mathbf{\Delta z}_i - \mathbf{d}_i)^{\mathrm{T}} \mathbf{R}_i^{-1}(\mathbf{H}_i\mathbf{\Delta z}_i - \mathbf{d}_i) + J_{\mathrm{c}}(\mathbf{\Delta z}_0)$$

$$\mathbf{d}_i = \mathbf{y}_i^{\mathrm{o}} - H_i(\mathbf{z}_i^{\mathrm{b}})$$

$$\mathbf{z}_{i+1}^{\mathrm{b}} = M_i(\mathbf{z}_i^{\mathrm{b}}) = M_i(M_{i-1}(M_{i-2}(\cdots M_0(\mathbf{z}_0^{\mathrm{b}}))))$$

$$\mathbf{\Delta z}_{i+1} = \mathbf{M}_i\mathbf{\Delta z}_i = \mathbf{M}_i\mathbf{M}_{i-1}\mathbf{M}_{i-2}\cdots\mathbf{M}_0\mathbf{N}\mathbf{\Delta z}_0$$

where $\mathbf{y}^{\circ}$ is observations, $\mathbf{z}^{\mathrm{b}}$ is the background, and $\mathbf{B}$ and $\mathbf{R}$ are the background error covariance and observation error matrices, M and $\mathbf{M}$ are the model operator and its linearization, H and $\mathbf{H}$ are the observation operator and its linearization, J_{c} is the penalty term to suppress gravity waves, and $\mathbf{N}$ is a nonlinear normal-mode initialization operator. The subscript i denotes a time slot, and n is the last one (JMA 2013b). The state vector $\mathbf{z}$ contains the atmospheric state as well as VarBC parameters, which is applied to satellite radiances. The observation operator H simulates observations from the model state and consists of spatial interpolation from neighboring grid points to observation points, conversion from model variables to observation quantities with a radiative transfer model and the like, and VarBC.

a. 4D-Var

4D-Var has a significant advantage over 3D-Var, which was used for JRA-25, in using a forecast model to propagate initial perturbations and in prop-

Table 5. Data assimilation systems used for JRA-25 and JRA-55.

	JRA-25	JRA-55
Base system	JMA's operational system as of March 2004 (JMA 2002)	JMA's operational system as of December 2009 (JMA 2007, 2013b)
Horizontal grid system	Gaussian	Reduced Gaussian
Horizontal resolution	T106 (~110 km)	TL319 (~55 km)
Atmospheric analysis		
Vertical levels	Surface and 40 levels up to 0.4 hPa	Surface and 60 levels up to 0.1 hPa (Iwamura and Kitagawa 2008; Nakagawa 2009)
Analysis scheme	3D-Var with the T106 inner resolution	4D-Var with the T106 inner resolution
Background error covariances	Static	Static with the simple inflation factor of 1.8 applied before 1972
Bias correction for satellite radiances	TOVS Adaptive scheme using 1D-Var analysis departures (Sakamoto and Christy 2009) ATOVS Static (until July 2009) and adaptive (thereafter) schemes using radiosonde and supplemental background fields (Kazumori et al. 2004)	VarBC (Derber and Wu 1998; Dee and Uppala 2009; JMA 2013b)
Radiative transfer model for satellite radiances	TOVS: RTTOV-6 ATOVS: RTTOV-7	RTTOV-9.3
Surface analysis		
Screen-level analysis	2D-OI	2D-OI with the FGAT approach
Land surface analysis	Offline SiB with 6-hourly atmospheric forcing	Offline SiB with 3-hourly atmospheric forcing
Snow depth analysis	2D-OI	2D-OI

erly taking account of observation time, both of which are beneficial for producing analysis fields with greater physical consistency. On the other hand, 4D-Var requires greater computer resources because time integration of the forecast model is performed as part of the iteration to minimize the cost function J. To reduce the computational cost, analysis increments are produced with the T106 resolution model, while first guess fields are produced with the TL319 resolution model in JRA-55 (JMA 2007). Minimization of the cost function J is done using the limited-memory Broyden-Fletcher-Goldfarb-Shanno (BFGS) algorithm (Liu and Nocedal 1989) employing the preconditioner by Veersé et al. (2000).

b. Background error covariances

The background error covariance model used for JRA-55 is the same that was used for JRA-25 (JMA 2007), which is similar to the formulation by Derber and Bouttier (1999). In this formulation, the control variables consist of relative vorticity, unbalanced divergence, unbalanced mass (temperature and surface pressure), and the logarithm of specific humidity, which are represented in spectral space for each model level. The model variables are recovered from control variables, which takes into account the geostrophic balance with relative vorticity and the correlation between unbalanced divergence and the mass variables. There is no correlation between different spectral coefficients but a full vertical auto-

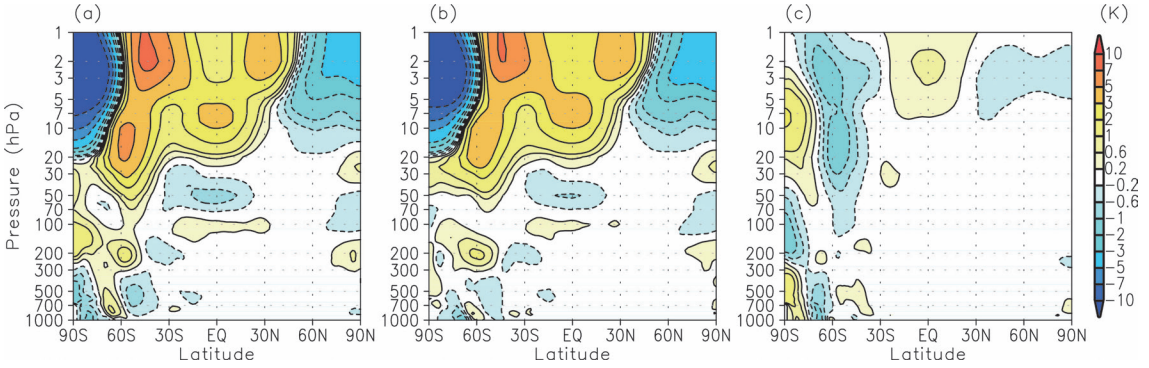

Fig. 6. Zonal mean differences between temperature analyses of (a) observing system experiments with and without satellite observations, (b) the same as (a) but using background error variances multiplied by 1.8 for the reduced observing system experiment and (c) reduced observing system experiments with the original and inflated background error variances, averaged over August 1990.

covariance matrix is defined for each spectral coefficient. Therefore, the resulting autocovariance model is nonseparable and isotropic in grid space. There are three differences from the formulation by Derber and Bouttier (1999). First, weakening of the geostrophic balance in the tropics is taken into account by expressing the regression equations in singular vector space instead of spectral space. Second, the logarithm of specific humidity, instead of specific humidity, is used as a control variable. Third, error variances are horizontally constant because variance adjustment is not performed in grid space.

The background error covariances and regression coefficients used for JRA-55 were statistically computed using the NMC method (Parrish and Derber 1992) on 24/48-h forecast differences for a year from October 2004.

Although the background error covariance matrix **B** used for JRA-55 is static, it was increased by 80 % for the pre-satellite period before 1972 for all the control variables except the logarithm of specific humidity to account for the increased background errors. This scaling factor was obtained using the diagnostics by Desroziers et al. (2005) on departures from observing system experiments with and without satellite observations for January and August 1990. Figure 6 shows that the difference between zonal mean temperature analysis fields is slightly reduced by the adjustment of background error variances.

c. *VarBC*

To effectively assimilate satellite radiances, it is necessary to properly remove biases stemming from incomplete instrument calibration or radiative transfer modeling. Because these biases depend on time and atmospheric state in most cases, bias estimates need to be continuously updated to adapt to the actual biases. VarBC uses the state vector **z** augmented with bias parameters, and thereby automatically adjusts bias estimates to maintain consistency with all available information in the cost function J (Derber and Wu 1998; Dee and Uppala 2009; JMA 2013b). In JRA-55, VarBC is applied to all satellite radiances.

d. *Radiative transfer model for satellite radiances*

Satellite radiances are assimilated using the software package Radiative Transfer for the TIROS Operational Vertical Sounder (RTTOV) version 9.3 (Saunders et al. 2008). Compared with RTTOV-6, which was used for assimilating TOVS data in JRA-25, it reproduces line-by-line radiances and Jacobians for the water vapor channels of HIRS with significantly improved accuracy (Matricardi et al. 2004). The simulation of ocean surface emissivity for microwave instruments at large viewing angles has also been significantly improved (Saunders 2002). Compared with RTTOV-7 (Matricardi et al. 2004), which was used for assimilating Advanced TOVS (ATOVS) data in JRA-25, it reduces systematic biases in calculated brightness temperatures for microwave water vapor channels. In addition, the removal of an inaccurate representation of the Zeeman effect has significantly improved the simulation for microwave upper stratospheric temperature channels (Kobayashi et al. 2009).

3.2 Surface analysis

a. Screen-level analysis

The analysis of screen-level variables (2-m temperatures, 2-m relative humidities and 10-m winds) is performed separately from the atmospheric analysis component. These variables are analyzed with a univariate 2-dimensional optimal interpolation (2D-OI). In JRA-25, departures were estimated by comparing observations with the first guess at the analysis time. In JRA-55, observations are compared with the first guess at the actual observation time and the departures are applied at the analysis time (the so-called first guess at the appropriate time (FGAT) approach).

Temperature and wind observations from islands are not used because they are not necessarily representative at the grid scale of JRA-55. Determining whether an observation is from an island is based on the 0.25-degree resolution land cover data; consequently, observations from the coast are also excluded.

Screen-level analysis fields are not used as initial conditions for forecasts.

b. Land surface analysis

Land surface analysis fields are generated by driving an offline version of the JMA Simple Biosphere (SiB) model with forcing fields from the atmospheric model, which is the same method used for JRA-25 (Onogi et al. 2007). Atmospheric forcing parameters are the same as those used for JRA-25, i.e., pressure, temperature, humidity, and wind at the lowest level of the atmospheric model, plus surface pressure, precipitation, downward solar and longwave radiation fluxes, and total cloud cover. Atmospheric forcing fields have 3-hour resolution in JRA-55 rather than 6-hour resolution in JRA-25. This change more realistically represents the diurnal cycles of atmospheric forcing.

The snow depth field in the land surface analysis at 00 UTC is replaced with a snow depth analysis field every day.

c. Snow depth analysis

Snow depth analysis fields are generated once a day with 2D-OI using SYNOP snow depth observations, which is the same method as the one used for JRA-25 (Onogi et al. 2007). First-guess fields are derived for each grid point using (A) snow depth of the land surface analysis and (B) satellite snow covers, as follows:

- If there is snow in both (A) and (B), then (A) is assigned to the first guess.
- If there is snow only in (B), then the first guess is a snow depth that can bring the ground temperature down to the freezing point through melting (2.1 cm at the maximum).
- If there is snow only in (A), then the first guess is 0 cm.
- If there is no snow in (A) and (B), then the analysis is 0 cm without 2D-OI.

In addition, first-guess fields over ice sheets are replaced with either climatology or 2 cm, whichever is greater, in every analysis. This is because the offline SiB does not take into account the physical processes of ice sheets, and consequently snow over ice sheets tends to accumulate over time.

Satellite snow covers are retrieved in the 0.25° × 0.25° latitude/longitude grid from microwave imager radiances with the same scheme as used for JRA-25 (Onogi et al. 2007). In the algorithm, regions where the observation satisfies the following criteria are considered to be covered by snow:

$$T_{\mathrm{b}}(19\ GHz,\ \mathrm{H}) < 265\ K$$

$$T_{\mathrm{b}}(19\ GHz,\ \mathrm{H}) - T_{\mathrm{b}}(37\ GHz, \mathrm{H}) < \mathrm{threshold}(\mathrm{H})$$

$$T_{\mathrm{b}}(19\ GHz,\ \mathrm{V}) - T_{\mathrm{b}}(37\ GHz,\ \mathrm{V}) < \mathrm{threshold}(\mathrm{V})$$

where T_{b} is the brightness temperature, H and V are the horizontal and vertical channels, respectively. Thresholds (H, V) should be 0 K for ideal snow but in practice need to be adjusted depending on the snow and surface condition. Accordingly, those values were determined for each region, vegetation, and month. For periods when no snow cover retrieval is available, monthly climatology for the period 1987–2000 is used instead.

4. Forecast model

A forecast model is employed to run forecasts using the most recent previous analysis as its initial condition, generating the background and atmospheric forcing fields that are necessary for analysis. A forecast model serves to propagate information of observations in time and place, and therefore its performance has a considerable impact on the quality of a reanalysis. The forecast model used for JRA-55 is based on the TL319 spectral resolution version of the JMA global spectral model (GSM) as of December 2009 (JMA 2007, 2013b), which has been extensively improved since JRA-25 (Table 6). The following subsections describe the major changes in the forecast model since JRA-25.

Table 6. Forecast models used for JRA-25 and JRA-55.

	JRA-25	JRA-55
Base model	JMA GSM as of March 2004 (JMA 2002)	JMA GSM as of December 2009 (JMA 2007, 2013b)
Horizontal resolution	T106 (~110 km)	TL319 (~55 km)
Vertical levels	Surface and 40 levels up to 0.4 hPa	Surface and 60 levels up to 0.1 hPa (Iwamura and Kitagawa 2008; Nakagawa 2009)
Dynamics		
Horizontal grid system	Gaussian	Reduced Gaussian
Advection scheme	Euerlian	Semi-Lagrangian
Radiation		
Longwave radiation	*Line absorptions* Random band model of Goody (1952) *Water vapor continuum (e-type)* Roberts et al. (1976) *Radiatively active gases* H_2O, O_3 and CO_2 (constant at 375 ppmv)	*Line absorptions* Pre-computed transmittance tables and k-distribution (Chou et al. 2001) *Water vapor continuum (e-type and p-type)* Zhong and Haigh (1995) with MK_CKD (Clough et al. 2005) *Radiatively active gases* H_2O, O_3, CO_2, CH_4, N_2O, CFC-11, CFC-12 and HCFC-22
Shortwave radiation	*Absorptions by H_2O, O_2, O_3 and CO_2* Briegleb (1992)	*Absorptions by H_2O* Briegleb (1992) *Absorptions by O_2, O_3 and CO_2* Freidenreich and Ramaswamy (1999)
Cloud radiation	*Longwave* Maximum-random overlap *Shortwave* Random overlap	*Longwave* Maximum-random overlap with the method of Räisänen (1998) *Shortwave* Random overlap
Aerosols	Atmospheric aerosol profiles from WMO (1986) (CONT-I over land and MAR-I over sea)	Atmospheric aerosol profiles from WMO (1986) (CONT-I over land and MAR-I over sea) with optical depths adjusted to 2-dimensional monthly climatology
Cumulus convection	Prognostic Arakawa-Schubert	Prognostic Arakawa-Schubert with DCAPE
Initialization	Nonlinear normal mode initialization	Not used
Boundary conditions and forcing fields		
SST and sea ice	COBE-SST (Ishii et al. 2005)	COBE-SST (Ishii et al. 2005)
Ozone	T42L45 version of MRI-CCM1 (Shibata et al. 2005)	*Until 1978* Climatology *From 1979 onward* T42L68 version of MRI-CCM1 (Shibata et al. 2005)

4.1 Dynamics

To mitigate the overconcentration of grid points at high latitudes and lower the computational cost, a reduced Gaussian grid is adopted for the GSM. The number of grid points at each latitude is determined from the magnitude of associated Legendre functions, which is negligibly small at high latitudes and in high orders. This method also reduces the computational cost of Legendre transformation (Juang 2004; JMA 2013b).

GSM is constructed on the framework of a semi-implicit semi-Lagrangian global model. The general shortcomings of semi-Lagrangian models are the lack of conservation properties and the heavy cost of three-dimensional interpolations. To address these limitations, Yoshimura and Matsumura (2003) developed a vertically conservative semi-Lagrangian scheme in which vertical advection is treated separately from horizontal advection, so that the model may preserve the conservation of vertically integrated quantities, such as water vapor, under non-dissipative conditions. The separate treatment enables the model to reduce the cost of interpolations and to recover the conservative property (JMA 2013b).

4.2 Radiation

a. Longwave radiation

Longwave radiation fluxes are computed by solving the equation of radiative transfer for a non-scattering atmosphere in each predefined spectral band (the band-emissivity method with the diffusivity approximation). To reduce the computational costs, computations for longwave radiation are performed not at every time step but every three hours (JMA 2007).

In the forecast model used for JRA-25, the longwave spectrum was divided into 4 bands. Band-averaged transmission functions were obtained using the random band model of Goody (1952) for line absorptions by atmospheric gases. The transmittances due to water vapor continuum absorption were computed with the expression by Roberts et al. (1976), which only considered the self (*e*-type) continuum resulting from collisions between water vapor molecules (JMA 2002). In the forecast model used for JRA-55, the number of spectral bands increased to 9. The basic framework for computing band-averaged transmission functions was replaced with the method of Chou et al. (2001), which uses a combination of pre-computed transmission tables (Chou and Kouvaris 1991) and the *k*-distribution method (Arking and Grossman 1972) to compute the transmittances due to line absorption. The transmittances due to water vapor continuum absorption are computed with the expression by Zhong and Haigh (1995), considers the self continuum as well as the foreign (*p*-type) continuum resulting from collisions between water vapor and non-water molecules (JMA 2007).

The pre-computed transmittance tables are applied to the absorption bands that substantially contribute to cooling in the stratosphere and above, i.e., the 15 μm band of carbon dioxide, the 9.6 μm band of ozone, and major absorption bands of water vapor. The *k*-distribution method is applied to other absorption bands. The rationale for using different approaches for different absorption bands is as follows. Although the *k*-distribution method with linear pressure scaling is computationally very fast, it is not accurate in the low-pressure condition where the Doppler broadening of absorption lines is important. This is due to the fact that the linear pressure scaling used in the *k*-distribution method, which assumes Lorentz broadening as the dominant cause of line broadening, does not hold in the low-pressure condition. Compared to the forecast model used for JRA-25, absorptions due to Doppler broadening are more properly represented in that used for JRA-55 due to the use of transmittance tables pre-computed for a wide range of pressures and temperatures.

Absorbing gases considered in the forecast model used for JRA-25 were only water vapor, ozone, and carbon dioxide (constant at 375 ppmv). In the forecast model used for JRA-55, five species (methane, nitrous oxide, chlorofluorocarbon (CFC)-11, CFC-12, and hydrochlorofluorocarbon (HCFC)-22) are also taken into account. For ozone and long-lived greenhouse gases (carbon dioxide, methane, nitrous oxide, CFC-11, CFC-12, and HCFC-22), temporal variations are taken into account. Further detail is given in Subsections 4.4.c and 4.4.d.

The transmittance tables were computed using the High Resolution Transmission (HITRAN) compilation 2000 (Rothman et al. 2003) and the Line-by-Line Radiative Transfer Model (LBLRTM, Clough et al. 1992; Clough and Iacono 1995). Absorption coefficients due to water vapor continuum are based on the Mlawer–Tobin–Clough–Kneizys–Davies (MT_CKD) water vapor continuum absorption model (Clough et al. 2005).

b. Shortwave radiation

Shortwave radiation fluxes are computed by a two-stream method with the δ-Eddington approximation (Joseph et al. 1976; Coakley et al. 1983). To cut down on the computational costs, computations for

shortwave radiation are not performed at every time step but hourly (JMA 2007).

In the forecast model used for JRA-25, the shortwave spectrum was divided into 18 bands (seven bands for the ultraviolet, one band for the visible, and ten subbands for the *k*-distribution method for the near-infrared) based on Briegleb (1992). This method took into account the absorptions due to ozone in the ultraviolet and visible, oxygen (constant at 209, 490 ppmv) in the visible and near-infrared, carbon dioxide in the 2.7 and 4.3 μm bands and water vapor in the near-infrared, and the Reyleigh scattering (JMA 2002). In the forecast model used for JRA-55, these parameterizations were updated following Feidenreich and Ramaswamy (1999) except for absorptions due to water vapor. In this method, the number of spectral bands increased to 10 for the ultraviolet and 5 for the visible. In addition, absorption due to the Schumann-Runge O_2 band is taken into account (JMA 2007).

In the forecast model used for JRA-25, the land surface albedos (at the top of vegetative canopies) were derived by solving the equation of radiative transfer in vegetative canopies using the optical properties of Dorman and Sellers (1989). The ocean surface albedo was parameterized following Briegleb et al. (1986), and the sea ice surface albedos were fixed at 0.8 for the visible and at 0.4 for the near-infrared. In the forecast model used for JRA-55, the sea ice surface albedo is parameterized as functions of solar zenith angle and skin temperature, so that correlation (anti-correlation) with solar zenith angle (skin temperature) is taken into account. Reflectivity over deserts is parameterized as a function of solar zenith angle following Briegleb et al. (1986). In addition, the snow surface albedo over perennial land ice was modified and increased by about 10 %.

c. Cloud radiation

In the longwave flux calculations, clouds are basically treated as blackbodies. Cloud overlap between different vertical layers is represented assuming the maximum-random overlap (Geleyn and Hollingsworth 1979) with the method of Räisänen (1998), in which the effects of cloud cover and cloud emissivity on cloud overlap are considered separately (Kitagawa and Murai 2006). Räisänen (1998) pointed out that the combined use of effective cloud cover, i.e., the product of cloud cover and cloud emissivity, and maximum-random overlap leads to smaller cloud radiative forcings as vertical resolution becomes higher, and demonstrated that this dependence on vertical resolution can be significantly reduced by separately taking into account the effects of cloud cover and cloud emissivity. The cloud emissivity is parameterized as functions of cloud liquid water content, cloud ice content, and effective radius of cloud particles.

Cloud optical properties used in the shortwave radiation scheme, i.e., the cloud optical depth, the single scattering albedo, and the asymmetry factor, are parameterized as functions of cloud water path and effective radius of cloud particles according to Slingo (1989) for water droplets and Ebert and Curry (1992) for ice crystals (JMA 2007). Cloud overlap in the shortwave is represented assuming random overlap.

In the forecast model used for JRA-25, the effective radius for water droplets was fixed at 15 μm, and that for ice crystals was parameterized as functions of temperature following Ou and Liou (1995) (JMA 2002). In the forecast model used for JRA-55, the effective radii for water droplets are fixed at 10 μm over land and at 13 μm over sea, and that for ice crystals is parameterized as functions of temperature and cloud ice content following Wyser (1998) (JMA 2007).

d. Aerosols

The aerosol direct effect is taken into account using two atmospheric aerosol profiles from WMO (1986), i.e., CONT-I over land and MAR-I over sea, which are basically the same profiles as those used for JRA-25. While no temporal variation was taken into account in JRA-25, JRA-55 uses a 2-dimensional monthly aerosol optical depth climatology, which is based on observations from the Moderate Resolution Imaging Spectroradiometer (MODIS) and the Total Ozone Mapping Spectrometer (TOMS) (JMA 2013b).

4.3 Cumulus convection

The basic framework of the cumulus convection scheme is the same that was used for JRA-25 (Onogi et al. 2007), which is an economical version of the Arakawa-Schubert scheme (Arakawa and Schubert 1974), except that JRA-55 uses the convective triggering mechanism proposed by Xie and Zhang (2000), known as the dynamic CAPE generation rate (DCAPE) (JMA 2013b).

4.4 Boundary conditions and forcing fields

a. Sea surface temperature (SST)

The SST analysis for JRA-55 is the Centennial In Situ Observation-based Estimates of the Variability of SSTs and Marine Meteorological Variables (COBE, Ishii et al. 2005), which is basically the same one used for JRA-25.

The SST analysis has a resolution of 1° latitude and 1° longitude and uses the OI method. The deviation of the previous day's analysis from normal, multiplied by 0.95, is used as a first guess. The analysis is performed daily and uses the marine meteorological data for the 7-day period from 3 days before to 3 days after the day of interest. The observed data in a day are averaged in a 1.5° × 1.5° box before analyzing data by the OI method (JMA 2007).

b. Sea ice

Sea-ice concentrations used for JRA-55 are basically daily data produced for COBE-SST, which are the same as for JRA-25. The sea-ice concentrations consist of data from Walsh and Chapman (2001) for the northern hemisphere and climatology for the southern hemisphere for the period before October 1978, and microwave imager retrievals by Matsumoto et al. (2006) thereafter. The data by Walsh and Chapman (2001) lack sea/lake-ice concentrations in the Sea of Okhotsk, the Gulf of St. Lawrence, and the Great Lakes for most of the period before October 1978, but no correction is made for COBE-SST. In JRA-55, climatology in those regions for the period 1979–1986 was used instead for the period before October 1978.

In the forecast model, regions where the sea-ice concentration exceeds 55 % are considered to be completely covered by sea ice and lower values are interpreted as zero sea-ice coverage.

c. Ozone

Three-dimensional daily mean ozone distributions used in JRA-55 for the period after 1979 were produced separately from the JRA-55 data assimilation system using the T42L68 resolution version of the chemistry climate model (CCM) developed at the Meteorological Research Institute (MRI-CCM1, Shibata et al. 2005). A nudging scheme was employed to assimilate total column ozone retrievals from TOMS on *Nimbus-7* and other satellites for the period 1979–2004 and from the Ozone Monitoring Instrument (OMI) on *Aura* thereafter. The ozone profiles were adjusted for each model grid point once a day at the solar culmination time using these observations. More detail is presented in the chemical transport model section in JMA (2013b). Wind fields were also nudged toward 6-hourly wind fields from JRA-25 to simulate the transport of chemical species in MRI-CCM1 as realistically as possible. In addition, the time evolution of total chlorine and bromine were prescribed in the CCM to incorporate the effects of ozone-depleting substances since 1979 (see Kobayashi and Shibata, 2011 for details). This method was the same as the one used for producing ozone distributions for JRA-25 (Maki et al. 2008).

The daily ozone distributions before 1978 were time-interpolated, three-dimensional climatological monthly means for 1980–1984.

d. Long-lived greenhouse gases

It is important to accurately represent radiative forcing due to the increase in long-lived greenhouse gases in forecast models. In the forecast model used for JRA-25, only carbon dioxide was taken into account, and its concentration was fixed at 375 ppmv. The forecast model used for JRA-55 takes six species into account (carbon dioxide, methane, nitrous oxide, CFC-11, CFC-12, and HCFC-22). Their concentrations are globally uniform and temporally varied based on the data sources listed in Table 7.

5. Production

The production of JRA-55 took about three years and was completed in March 2013. Since then, it has operated on a near-real-time basis as a successor to the previous JRA-25-based JMA Climate Data Assimilation System (JRA-25/JCDAS). JRA-55 was first run using eight nodes of the high-performance computer (Hitachi SR11000 model J1) in JMA's eighth-generation computer system with a peak performance of 121.6 GFLOPS per node (JMA 2007). After June 2012, it was continued with 16 nodes of the high-performance computer (Hitachi SR16000 model M1) in JMA's ninth-generation computer system with a peak performance of 0.98 TFLOPS per node (JMA 2013b). As the data assimilation system consists of numerous programs with complicated dependencies on one another, the Supervisor Monitor Scheduler (SMS) developed by ECMWF is used to efficiently control production tasks.

Initially, the reanalysis period was divided into two streams (A002, B002). The following technical problems were found at that time, which were corrected by recalculations (Fig. 7):

- From January to June 1958 (A003): Lack of sea/lake-ice data in the Sea of Okhotsk, the Gulf of St. Lawrence, and the Great Lakes.
- From December 1974 to August 1980 (A004): Problem in cloud detection for VTPR radiances.
- From June 1987 to September 1992 (B003): Misplacement of microwave imager snow cover retrievals.

Consequently, the streams shown in Fig. 7 have

Table 7. Data sources of long-lived greenhouse gases.

Molecule	Period	Source
CO_2	1958	Law Dome ice core data (Etheridge et al. 2008)
	1959–1982	Keeling Mauna Loa observations
	1983–2010	WDCGG (WMO 2012)
	2011–	RCP4.5 (Clarke et al. 2007; Smith and Wigley 2006; Wise et al. 2009)
CH_4	–1983	20C3M (Meinshausen et al. 2011)
	1984–2010	WDCGG (WDCGG 2012)
	2011–	Constant at the value in 2010
N_2O	–1979	20C3M (Meinshausen et al. 2011)
	1980–2010	WDCGG (WDCGG 2012)
	2011–	RCP4.5 (Clarke et al. 2007; Smith and Wigley 2006; Wise et al. 2009)
CFC-11, CFC-12, HCFC-22	–2005	20C3M (Meinshausen et al. 2011)
	2006–	A1 scenario of the Scientific Assessment of Ozone depletion: 2010 (WMO 2010)

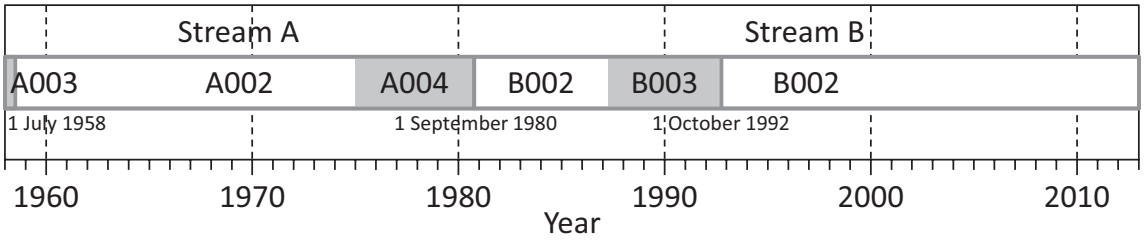

Fig. 7. Streams of JRA-55 production. Shading indicates periods during which recalculation was performed. Solid vertical lines indicate the times of three discontinuities (see text).

three discontinuities: at 00 UTC on 1 July 1958 (A003/A002), 00 UTC on 1 September 1980 (A004/B002), and 00 UTC on 1 October 1992 (B003/B002). For other stream changeovers, succeeding streams were initiated from the last data of the preceding streams.

6. Basic performance of the data assimilation system

6.1 Background and analysis fits to observations

Data assimilation systems produce not only analyses but also background and analysis departures (observations minus background and observations minus analysis). These departures contain plenty of information that is useful for monitoring data assimilation cycles. In particular, background departures can be used for various purposes such as estimating biases in observations and investigating performance of the forecast model because they are independent of prescribed background and observation errors. Here, we compare the time series of global mean and root-mean-square (RMS) departure of radiosonde temperatures used in JRA-25 and JRA-55.

Global mean departures from JRA-25 at levels near 30 hPa clearly show a large cold bias in the lower stratosphere, especially for the period before 1998 when TOVS data were used (Fig. 8a). In JRA-55, the cold bias has been reduced significantly, which can be seen clearly from the improved consistency with radiosonde temperatures. This improvement was primarily achieved by the proper representation of absorptions due to the Doppler broadening in the revised longwave radiation scheme.

At levels near 250 hPa, global mean departures from JRA-25 exhibit large low-frequency variations (Fig. 8c). Global mean departures from JRA-55 do not exhibit such large variations but are biased in the negative direction, indicating a warm bias in the upper troposphere. Time series from JRA-55 also show a jump in July 2006; thereafter, the warm bias has been

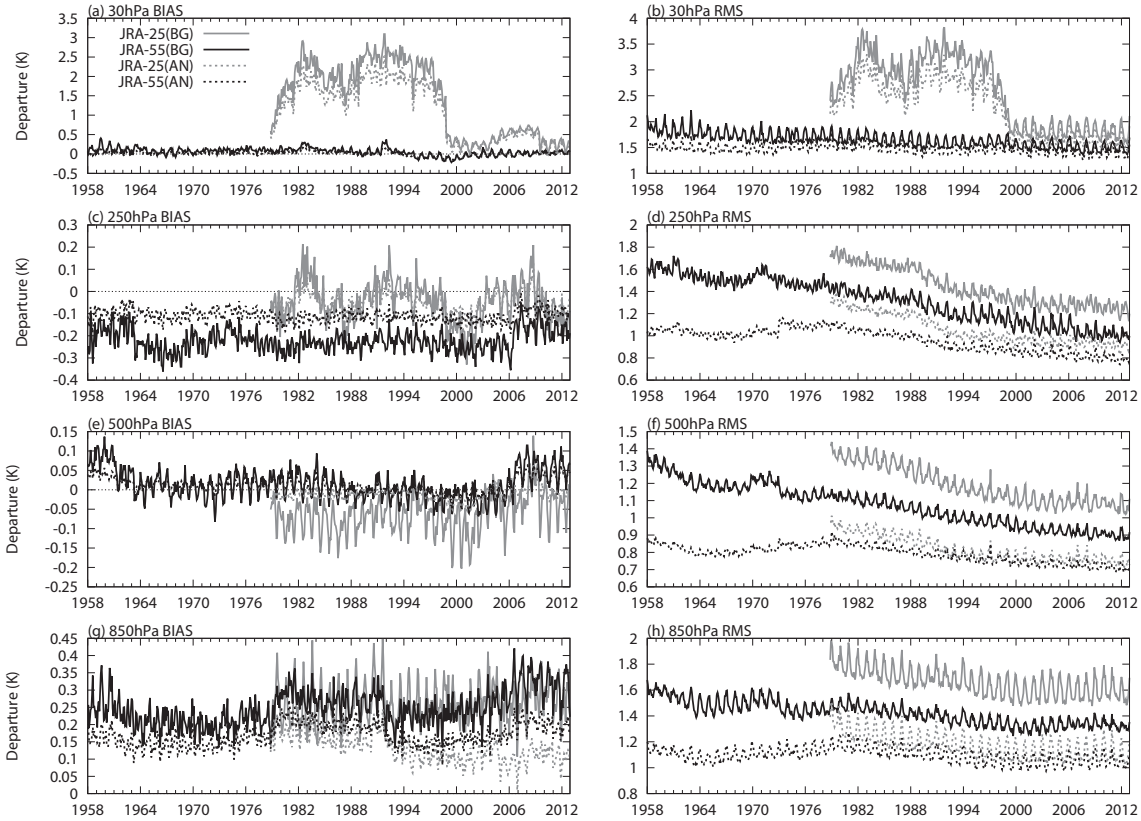

Fig. 8. Global mean and RMS departure of radiosonde temperatures used in JRA-25 and JRA-55. Solid lines show background departures, and dotted lines represent analysis departures.

reduced, which is most likely due to the assimilation of GNSS-RO observations.

At levels near 500 hPa, global mean departures from JRA-55 demonstrate an improved fit to radiosonde temperatures compared with those from JRA-25 (Fig. 8e), although they are slightly biased in the positive direction for the periods before the early 1960s and after the latter half of the 2000s. It can also be argued that smaller difference between RMS background and analysis departures in JRA-55 indicates smaller increments and is an evidence of improved physical consistency among analysis fields (Fig. 8f).

At levels near 850 hPa, global mean departures from both JRA-25 and JRA-55 are on the positive side throughout the reanalysis period (Fig. 8g), indicating a cold bias in the lower troposphere. These time series also exhibit shifts in the late 1970s, the early 1990s, and the mid-2000s. It must be noted that the number and distribution of samples for these statistics vary in time; therefore, these shifts might be attributed to apparent variations as well as the impacts of changes in observing systems. The causes of these shifts require further investigation.

6.2 Analysis increments

The analysis increment represents the extent to which observations affect the background through the data assimilation system. Although it does not necessarily represent errors in the background, its temporal variations provide useful insights regarding the impact of changes in observing systems on the temporal consistency of analyses.

Figure 9 compares time-height cross sections for the global mean monthly temperature increments from JRA-55 and JRA-25. The increments from JRA-55 are generally smaller than those from JRA-25, and they show fewer sudden changes in pattern following changes in observing systems. The difference between increments in JRA-25 and JRA-55 demonstrates a clear improvement of the model climatology and an advance in the bias correction methods for radiosonde temperatures and satellite radiances.

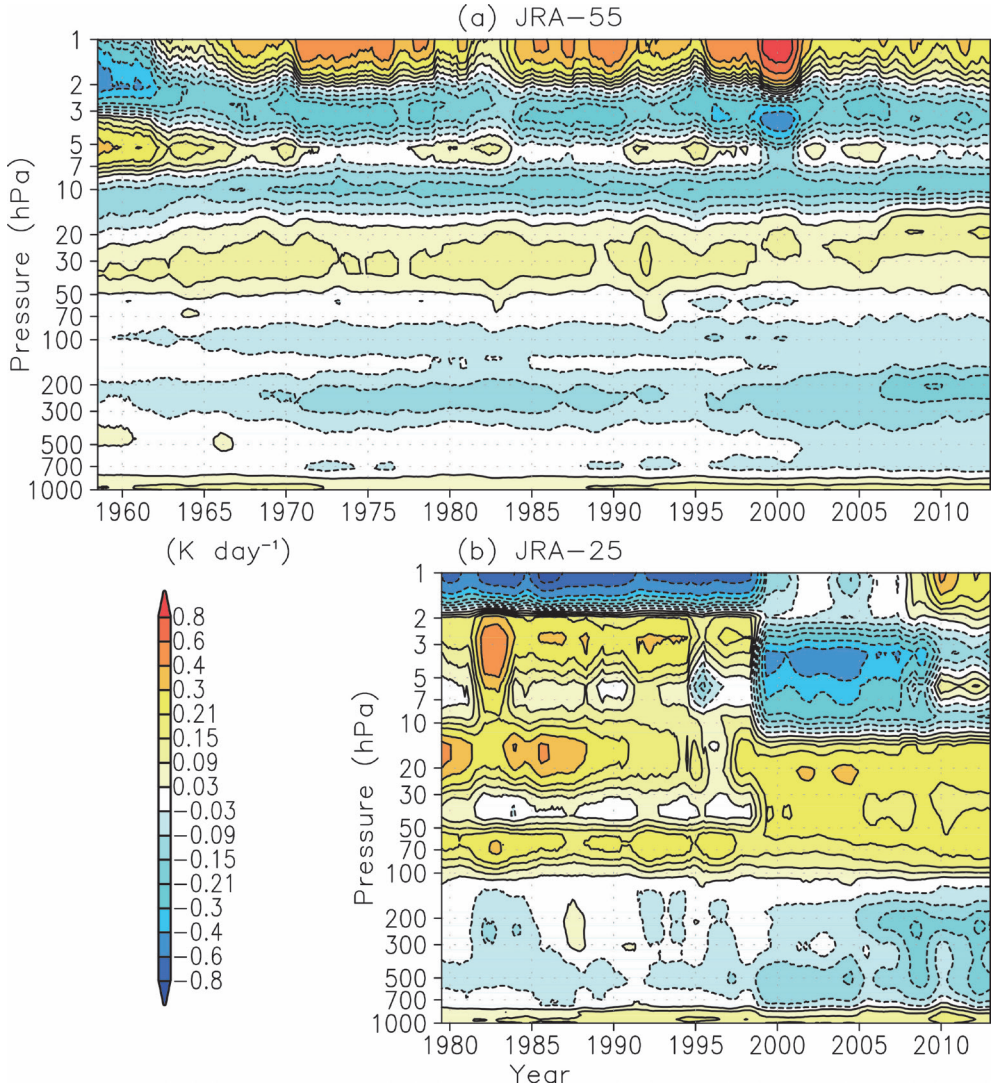

Fig. 9. Time-height cross sections for the 12-month running mean of the global mean temperature increments from (a) JRA-55 and (b) JRA-25.

However, there are cooling increments in the upper troposphere that gradually increase as the observing system is improved. The cooling increments are particularly apparent at levels near 200 hPa after July 2006 when the GNSS-RO refractivities were introduced into JRA-55. These signs indicate that the forecast model has a warm bias in the upper troposphere.

Another noticeable feature in Fig. 9 is an oscillatory structure in the vertical in the stratosphere. Modest variations can be observed in this structure before the early 1960s, during which few radiosonde observations were available in the upper stratosphere, and from August 1998 to December 2000, during which observations from TOVS and ATOVS were used at the same time. The variations in the increment structure suggest larger uncertainties in the upper stratospheric temperature analysis during these periods.

Figure 10 compares time-height cross sections for the global mean monthly specific humidity increments from JRA-55 and JRA-25. The increments from JRA-55 do not exhibit impacts of changes in observing systems as clear as those from JRA-25. However, JRA-55 has significant moistening increments above 850 hPa and drying increments below it, indicating that the forecast model has a dry bias

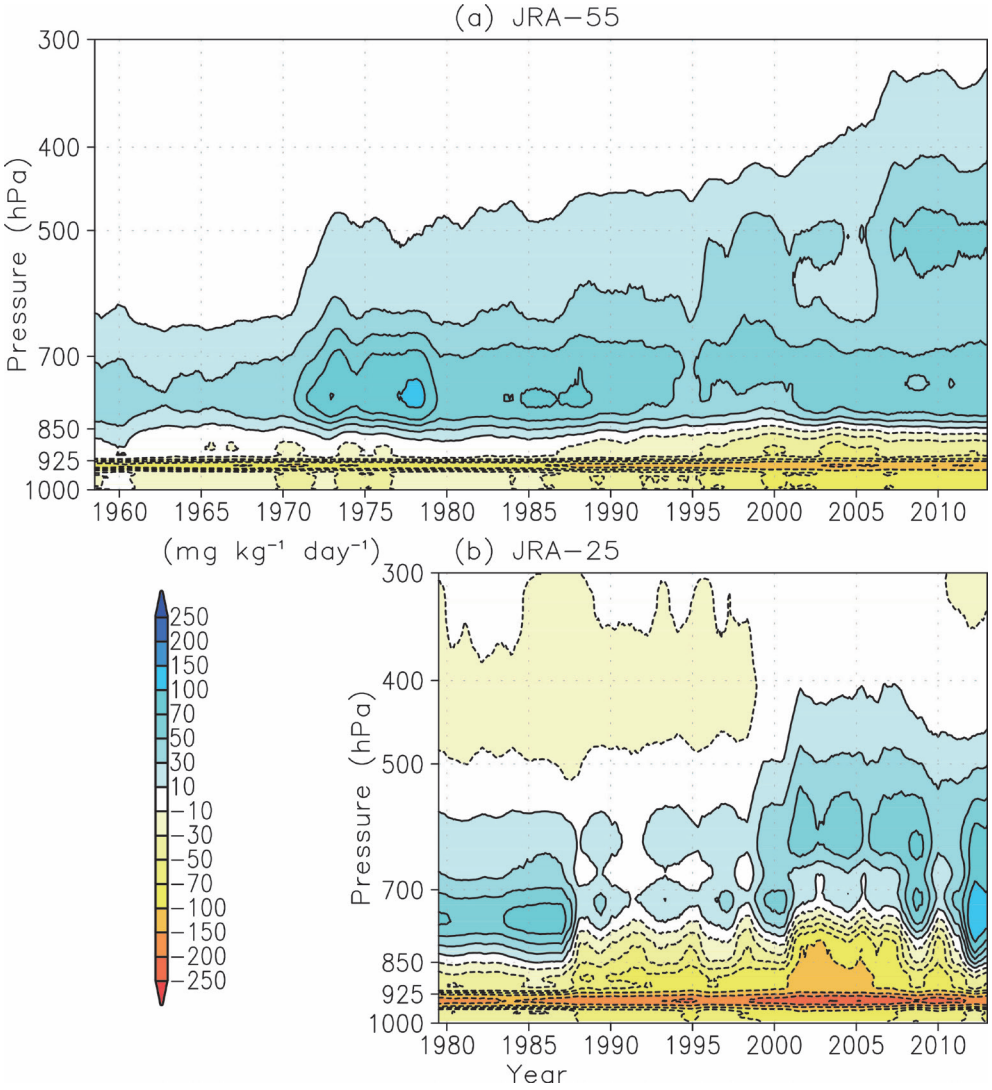

Fig. 10. Time-height cross sections for the 12-month running mean of the global mean specific humidity increments from (a) JRA-55 and (b) JRA-25.

in the upper and middle troposphere and a moist bias in the lower troposphere. The moistening increments in the upper and middle troposphere tend to slightly increase as the number of observations from satellite water vapor channels increases. Large moistening increments can also be seen around 800 hPa in boreal summer during 1971–1978, which are most likely because of miscoded radiosonde humidity observations and inadequate QC for radiances from the VTPR water vapor channel. Note that intense drying increments observed in the lower troposphere arise because supersaturations are removed in the analysis, whereas they are allowed in the forecast model such as in the regions where stratocumulus occurs.

Figure 11 shows precipitable water increments averaged over the periods 1958–1964 and 2002–2008. Humidity observations in the atmospheric analysis component of JRA-55 during the earlier period are only from radiosondes, whereas those during the later period consist of many satellite as well as radiosonde observations. As a result, the patterns of precipitable water increments in these periods look quite different, especially over the oceans, where extensive increments can be observed only in the later period. Comparison between precipitable waters from JRA-55 and independent microwave imager retrievals

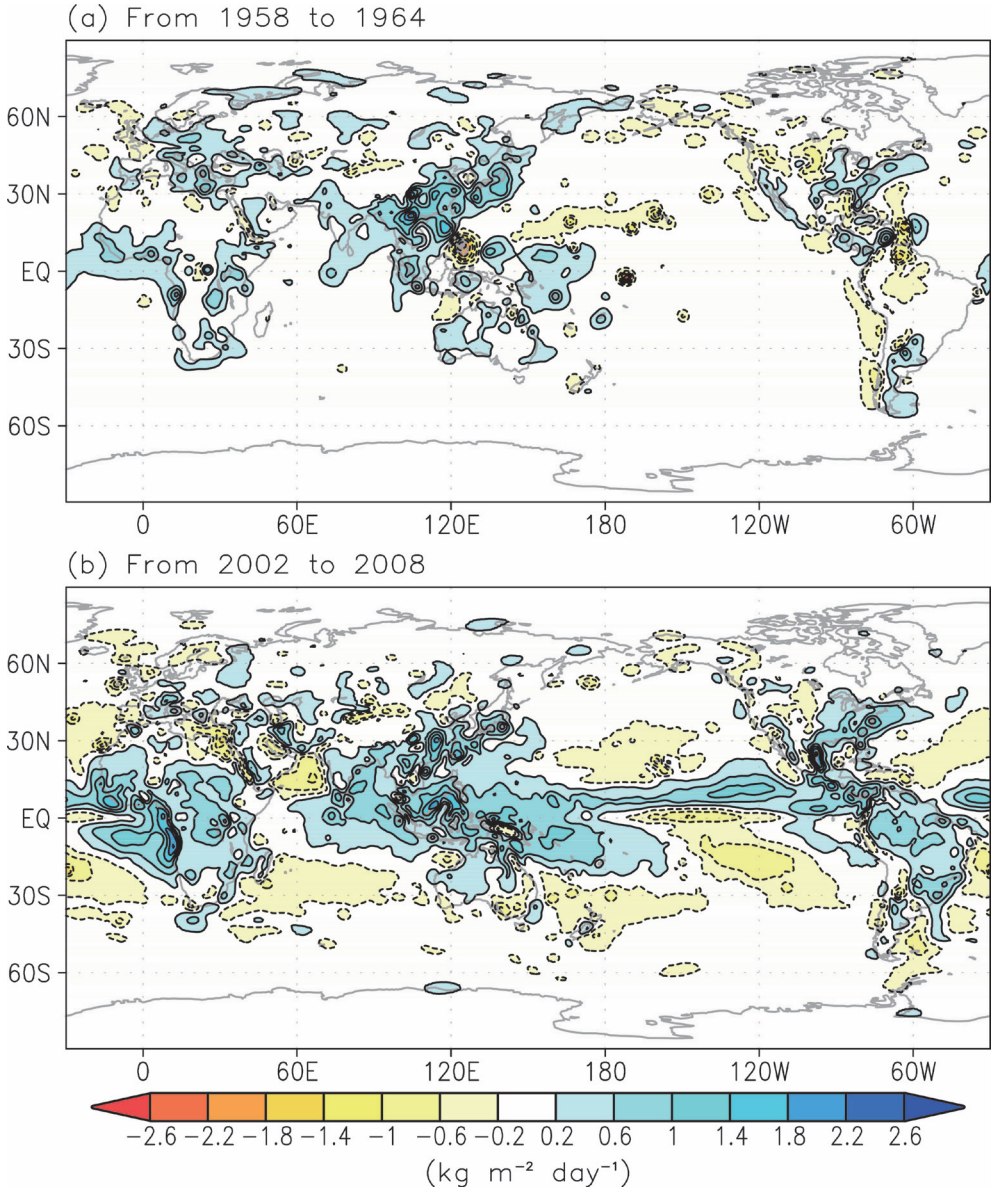

Fig. 11. Precipitable water increments averaged over the periods (a) 1958–1964 and (b) 2002–2008.

over the ocean indicates that the regions where large moistening increments occurred in the later period generally correspond to those where JRA-55 exhibits a dry bias (not shown). The increment pattern in 2002–2008 also suggests that the dry bias in the upper and middle troposphere seen in humidity (Fig. 10) is mainly from the regions of deep convection.

6.3 Two-day forecast scores

To evaluate the temporal consistency of the product and the impact of changes in observing systems, a short-range forecast was carried out in JRA-55 from 12 UTC every day. Figure 12 shows the time series of RMS errors in these 2-day forecasts at a geopotential height of 500 hPa averaged over the extratropical northern and southern hemisphere from JRA-25, JRA-55, and the JMA operational system, as verified against their own analyses. Because the forecasts were carried out with their own forecast models, the comparison is not made based on a common standard;

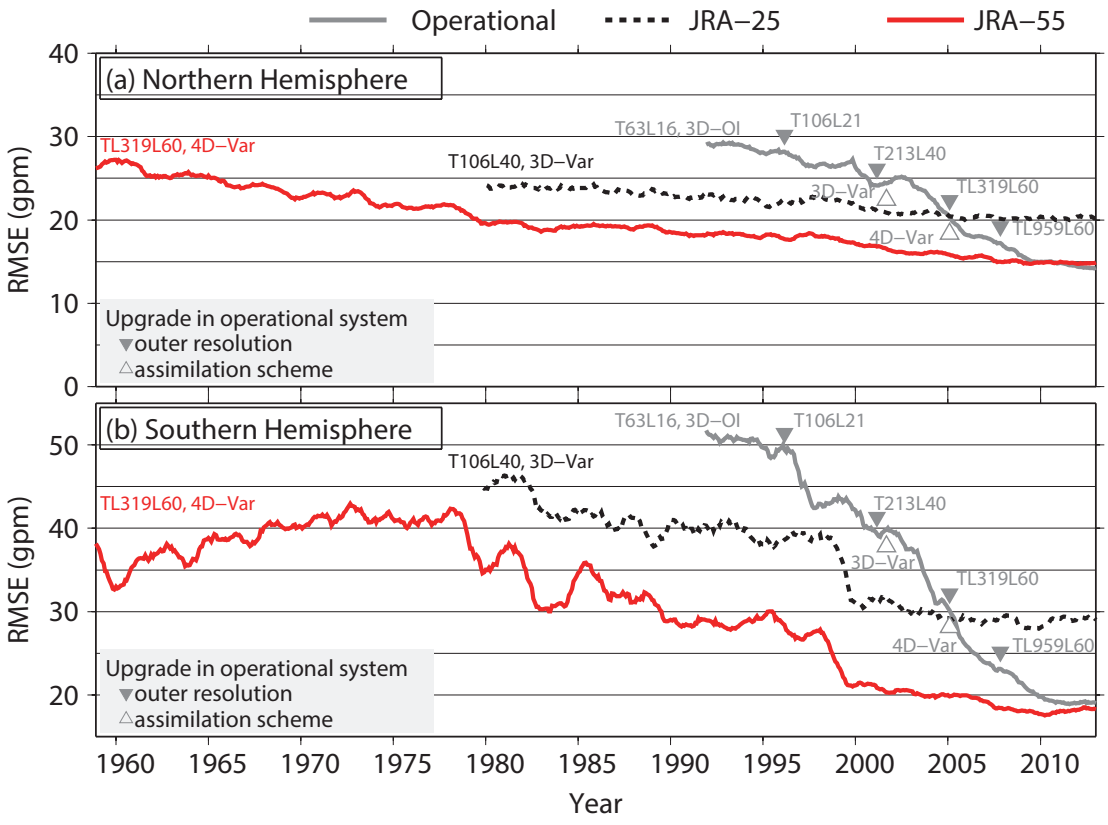

Fig. 12. RMS errors of 2-day forecasts of the geopotential height at 500 hPa averaged over the extratropics of the (a) Northern and (b) Southern Hemispheres from JRA-25, JRA-55, and JMA operational system, verified against their own analyses. Changes in the assimilation scheme and resolution of the outer model are also noted. Each value represents the average for the last 12 months.

nevertheless, it can provide useful insights regarding the temporal consistency of each product.

The JMA operational system has been improved in many aspects since JRA-25, including a revision of the longwave radiation scheme and the introduction of 4D-Var and VarBC. The JRA-55 data assimilation system, which is based on the TL319 resolution version of the operational system as of December 2009, incorporates these improvements and has been used consistently throughout the reanalysis period. Thus, variations in the forecast scores of JRA-55 can be attributed solely to the changes in observing systems and natural variations of atmospheric predictability, whereas forecast scores of the operational system clearly show the effect of these improvements. These are evidence of the greater temporal consistency of the JRA-55 product. The forecast scores of the JRA-55 system are considerably better than those of the JRA-25 system, which is based on the T106 resolution version of the operational system as of March 2004. The improvement of forecast scores is particularly significant in the southern hemisphere, which is most likely because of the availability of new satellite observations as well as the improvement of the data assimilation system.

The forecast scores of JRA-55 show relatively large variations that correspond to the introduction of VTPR in 1973; the advent of satellite observing systems in the late 1970s, ATOVS in 1998, and GNSS-RO in 2006; and variations in coverage of TOVS observations, suggesting that performance under sparse observations is an important concern for future reanalyses. It should be noted that the forecast scores in the southern hemisphere tend to be degraded during the pre-satellite era, whereas the number of used obsevations rather increased (Figs. 2d, e). This inconsistency may indicate that the JRA-55 data assimilation system did not perform well during this

period.

7. Improvements from JRA-25

7.1 Temporal consistency of temperature analysis

The representation of low-frequency variability and trends has been a major issue for reanalysis. Recent investigations using new-generation reanalyses have indicated significant improvement in this respect (Santer et al. 2004; Simmons et al. 2004, 2010, 2014). As the first reanalysis of the full observing system covering the last half-century since ERA-40, JRA-55 is expected to be used for various purposes including studies of multidecadal variability and climate change, thus it is very important to evaluate its temporal consistency. In this section, we compare low-frequency variability and trends in global mean temperatures from JRA-55 with those from independent observational datasets and other reanalyses, including JRA-25.

a. Near surface over land

Figure 13 compares monthly mean land-surface air temperature anomalies from the Climatic Research Unit (CRU) temperature database (CRUTEM4, Jones et al. 2012), the NCEP/NCAR reanalysis, ERA-40, JRA-25, and JRA-55, averaged over the globe. Reanalyses are sampled with the same spatial and temporal coverage as CRUTEM4. The screen-level analysis method used for JRA-55 is basically the same as the one used for JRA-25, and the low-frequency variability of 2-m temperature anomalies over land is fairly similar in the two reanalyses. Compared with ERA-40, the trend reproduced in JRA-55 is closer to that in CRUTEM4 but there is a difference of less than 0.1 K in warming between CRUTEM4 and JRA-55 after the 1990s. The difference might be related to a difference in how observations are used in CRUTEM4 and JRA-55. Observations on islands and the coast are not used in the screen-level analysis of JRA-55, as mentioned in Subsection 3.2.a, and analysis in those areas could be affected by observations in coastal waters such as reports of surface observation from sea stations (SHIP) and buoy observations (BUOY), and by SST through background fields. CRUTEM4 is based on observations over land only, which include those on islands and on the coast.

b. Lower troposphere to lower stratosphere

Figure 14 compares monthly temperature anomalies from JRA-55, existing reanalyses, and independent observational datasets for four layers from the lower troposphere to the lower stratosphere, averaged

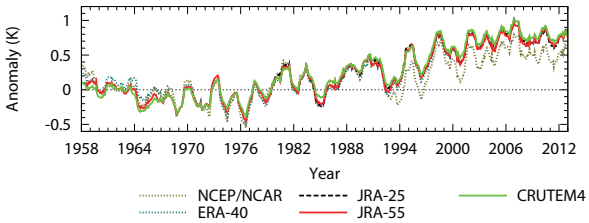

Fig. 13. Twelve-month running mean land-surface air temperature anomalies from CRUTEM4, the NCEP/NCAR reanalysis, ERA-40, JRA-25, and JRA-55, averaged over the globe. Anomalies for each dataset were defined relative to their own climatological monthly means over 1961–1990, except JRA-25, for which anomalies were first computed relative to its own climatological monthly means over 1981–2010 and then adjusted so that their average over 1979–1990 gave the same value as that of JRA-55. Reanalyses are sampled with the same spatial and temporal coverage as CRUTEM4.

over 82.5°N to 82.5°S. The independent observational datasets are the Hadley Centre's radiosonde temperature product (HadAT2, Thorne et al. 2005) and the Remote Sensing Systems (RSS) V3.3 atmospheric temperature records from the MSU and AMSU microwave sounders (Mears and Wentz 2009a, b).

The JRA-25 forecast model had a significant cold bias in the lower stratosphere, resulting in large artificial jumps after changes in observing systems or bias correction methods for satellite radiances. JRA-55 considerably reduces those changes; in particular, the time series for the three tropospheric layers before the 1970s shows variations very similar to those in HadAT2 compared with the NCEP/NCAR reanalysis and ERA-40.

For the lower stratosphere, the low-frequency variability reproduced in JRA-55 is closer to that in HadAT2 and RSS compared with other reanalyses, whereas the cooling trend observed in JRA-55 is smaller than that in HadAT2. McCarthy et al. (2008) investigated uncertainty in estimates of multidecadal trends in HadAT with an automated homogenization system, and suggested that the homogenization is likely to underestimate adjustments if observations from neighboring radiosonde stations have a common systematic bias. This could partly account for the difference in cooling trends between HadAT2 and JRA-55. In addition, RAOBCORE v1.4, which was used in JRA-55 until 2006, has a larger warming trend in the upper troposphere and a smaller cooling trend

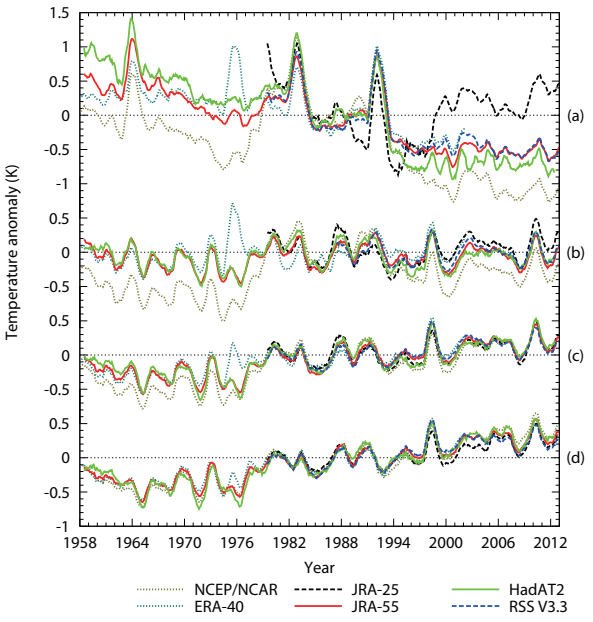

Fig. 14. Twelve-month running mean temperature anomalies for the (a) lower stratosphere, (b) upper troposphere, (c) middle troposphere, and (d) lower troposphere averaged over 82.5°N to 82.5°S. Time series from RSS V3.3 represents measurements by the MSU channel 4, 3, and 2, and the lower tropospheric extrapolations, whereas those from HadAT2, the NCEP/NCAR reanalysis, ERA-40, JRA-25, and JRA-55 are MSU equivalent brightness temperatures. Anomalies for each dataset were defined relative to their own climatological monthly means over 1979–1998.

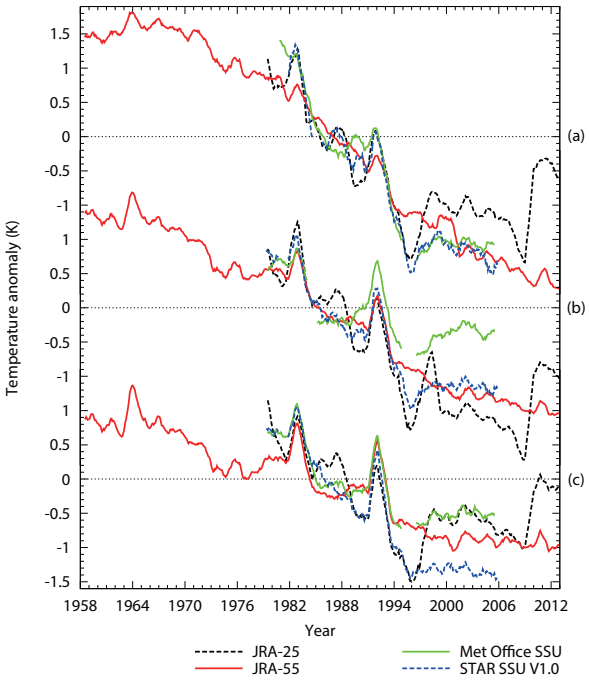

Fig. 15. Twelve-month running mean temperature anomalies for the (a) top, (b) upper and (c) middle stratosphere averaged over 75°N to 75°S. Time series from the Met Office SSU dataset and STAR SSU dataset V1.0 represent measurements by the SSU channels 3, 2, and 1, whereas those from JRA-25 and JRA-55 are SSU equivalent brightness temperatures. Anomalies for each dataset were defined relative to their own climatological monthly means over 1980–1994.

in the lower stratosphere than the latest version (v1.5) of RAOBCORE (Haimberger et al. 2012). Therefore, the possibility of underestimation of a cooling trend in JRA-55 cannot be ruled out.

c. Middle to top stratosphere

Figure 15 compares monthly temperature anomalies from JRA-25, JRA-55 and two independent observational datasets for the middle, upper, and top stratosphere, averaged over 75°N to 75°S. The independent datasets are the Met Office SSU dataset (Nash and Forester 1986; Nash 1988; Shine et al. 2008) and the National Oceanic and Atmospheric Administration (NOAA) the Center for Satellite Application and Research (STAR) SSU dataset version 1.0 (Wang et al. 2012). These two SSU datasets display strikingly different time series, suggesting a clear need for better understanding observational characteristics of the SSUs to obtain more reliable estimates of stratospheric temperature trends (Thompson et al. 2012). In JRA-55, radiances from all the channels of SSUs were directly assimilated with VarBC.

The impact of changes in observing systems on the JRA-55 time series is reduced compared with JRA-25 but the low-frequency variations are smaller than those of the SSU datasets, especially in the top stratosphere. The forecast model used for JRA-55 does not take into account interannual variations of volcanic aerosols, solar constant, and stratospheric water vapor concentrations. Because VarBC cannot distinguish between observational and forecast model biases, availability of anchoring observations such as radiosonde and GNSS-RO is a key factor in keeping analysis fields from drifting toward model clima-

tology. In the upper stratosphere and above, however, such observations are sparse. Consequently, VarBC only partially corrects biases in observations from stratospheric temperature channels, and even drifts towards the model climatology, showing smaller time variations in Fig. 15.

Trends represented in the two SSU datasets are in reasonable agreement in the top stratosphere, and JRA-55 time series also shows a similar trend. However, the time series for the middle and upper stratosphere show significant discrepancies between the two SSU datasets. Trends in JRA-55 are closer to the Met Office SSU dataset in the middle stratosphere and closer to the STAR SSU dataset in the upper stratosphere. These differences could be attributed to both uncertainty in the homogeneity of the SSU datasets and underestimation of the interannual variability in JRA-55. Unless their relative contributions are clarified, it is difficult to make further comments on reliability of any of these trends. From the viewpoint of reanalysis, the reliability of stratospheric temperature variations could be improved by taking account of the missing factors in the forecast model, correcting known problems in calibration (Nash and Saunders 2013) and improving radiative transfer modeling for upper stratospheric temperature channels (Kobayashi et al. 2009), thereby reducing the dependence on VarBC.

7.2 Representation of the South American monsoon system

In JRA-25, surface pressure observations with erroneous station heights generated spurious anticyclonic circulation anomalies in the lower troposphere over the Amazon basin, which resulted in a dry bias in this region (Fig. 16c). Accordingly, suspect observations were excluded from preliminary experiments for JRA-55. However, the anomalies did not disappear, and there still remained a dry bias in the South American monsoon region (Fig. 16d).

It is known that circulation patterns in the rainy season in this region are characterized by 1) water vapor transported southwest from the ocean into the continent and then transported southeast along the east side of the Andes to Bolivia and 2) water vapor carried around the edge of the South Atlantic subtropical high that flows into southeastern Brazil (Raia and Cavalcanti 2008). However, JRA-25 and preliminary experiments for JRA-55 both showed that water vapor fluxes into the continent were partly blocked by anticyclonic circulation increments (Figs. 16f, g), which appeared to partly account for the dry bias. Those anticyclonic anomalies stemmed from positive surface pressure increments, and intensified most at 18 UTC, the time at which mesoscale convective systems start to form in this region (early afternoon in local time) (Figs. 17a, b, c, d).

The root cause of the positive surface pressure increments has not been identified, but it might be related to biases in surface pressure observations, errors in station heights and the fact that the solar semidiurnal tide reproduced in the JMA GSM is about 10° of longitude ahead of the observed tide (D. Hotta 2010, personal communication). Surface pressure increments from JRA-55 experiments clearly exhibited a westward propagating component of wavenumber 2 in the tropics, of which peaks were located near the nodes of the solar semidiurnal tide. Another possible cause is that surface pressure observations in the sea surrounding South America are sparse, and consequently surface pressure increments tend to localize on land.

There may also be a feedback mechanism that reinforces positive surface pressure increments in the data assimilation system. Once the land surface is dried up, the increase in sensible heat flux causes warming in the lower troposphere, which results in decreased background surface pressures that in turn reinforce positive surface pressure increments. In addition, observational constraint on soil moisture in the land surface analysis of JRA-55 is imposed only by snow depths through snow depth analysis, which might be a reason why the feedback mechanism is maintained.

Because solving the root cause of this problem requires a long-term effort outside the scope of the JRA-55 project, we entirely excluded surface pressure observations over the Amazon basin. In an experiment with this solution, surface pressure increments over the Amazon basin mostly disappeared (Figs. 17e, f, g, h). The experiment also produced only small total column water vapor flux increments (Fig. 16h) and reproduced a precipitation distribution closer to those of the Global Precipitation Climatology Project (GPCP) version 2.2 (Adler et al. 2003) and the Global Precipitation Climatology Centre (GPCC) full data reanalysis version 6.0 (Schneider et al. 2011) (Figs. 16a, b, e).

8. Basic characteristics of JRA-55

8.1 Global energy budget

In reanalysis, the energy balance is not exactly preserved due to analysis increments. The degree to which the actual energy balance is reproduced can serve as an indicator of the quality and usability of the

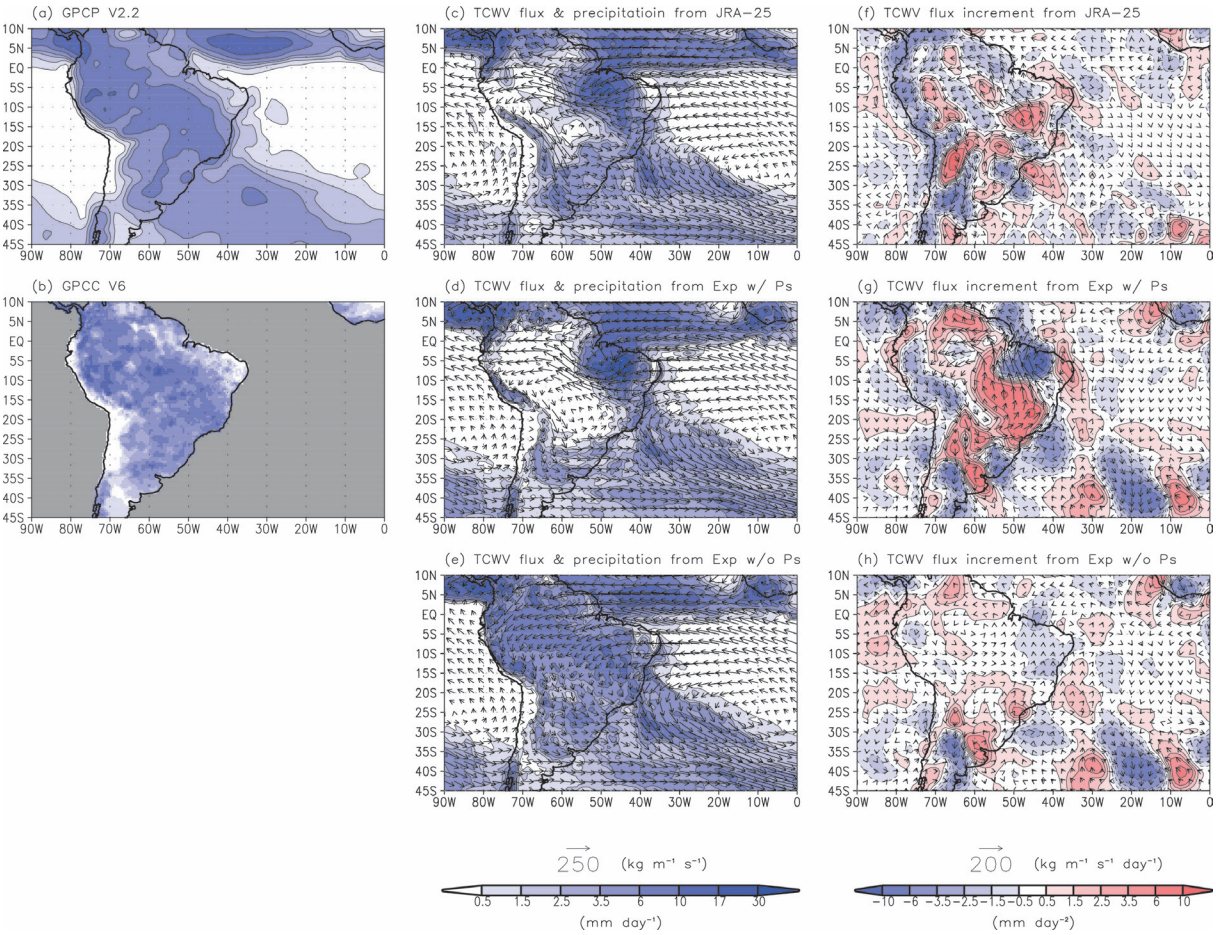

Fig. 16. (a–e) Monthly mean precipitation and (f–h) total column water vapor flux increments and their divergence from (a) GPCP V2.2, (b) GPCC V6, (c, f) JRA-25, and preliminary experiments for JRA-55 with surface pressure observations assimilated (d, g) and excluded (e, h) over the Amazon basin, averaged over November 1979. Total column water vapor flux analyses are also shown in (c–e).

reanalyses for many purposes (Trenberth et al. 2011). Observations related to Earth's energy balance have also substantial uncertainties, especially at the Earth's surface, where satellites cannot make direct measurements. Wild et al. (2013) proposed new best estimates for the components of the global mean energy balance along with their uncertainty ranges, which they estimated by combining surface observations from the global energy balance archive (GEBA) and the Baseline Surface Radiation Network (BSRN) with the radiation budgets from simulations performed in Coupled Model Intercomparison Project Phase 5 (CMIP5). Here, we evaluate the energy balance reproduced in JRA-55 using the estimates by Wild et al. (2013), and we examine differences from the Clouds and the Earth's Radiant Energy System (CERES) observations and JRA-25.

Tables 8 and 9 list the components of the global mean annual energy balance from Wild et al. (2013), JRA-25 and JRA-55 for the top of the atmosphere (TOA) and the Earth surface, respectively. The values of JRA-55 mostly are within the uncertainty ranges of Wild et al. (2013), except for the outgoing thermal flux, hydrological cycle components and net energy fluxes. The most notable change from JRA-25 is that the surface downward thermal flux is closer to the best estimate, most likely due to the improved representation of water vapor continuum absorption in the revised longwave radiation scheme.

The TOA reflected solar flux also becomes closer

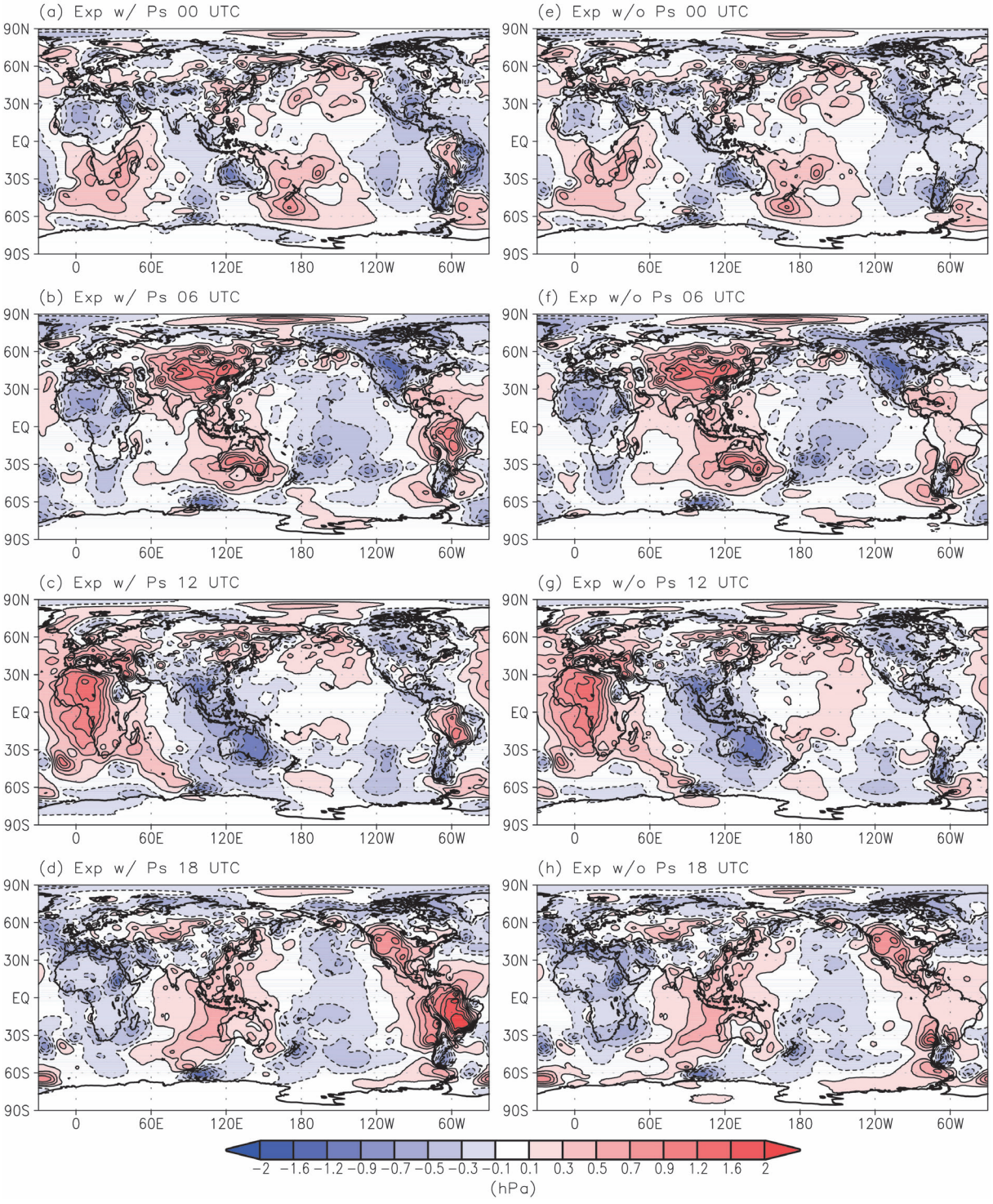

Fig. 17. Monthly mean surface pressure increments from preliminary experiments with surface pressure observations assimilated (a–d) and excluded (e–h) over the Amazon basin, averaged over (a, e) 00 UTC, (b, f) 06 UTC, (c, g) 12 UTC, and (d, h) 18 UTC data for November 1979.

Table 8. Global annual mean energy balance at the TOA (W m^{-2}). Values from JRA-25 and JRA-55 are for the period 2002–2008, whereas those from Wild et al. (2013) represent present-day climate conditions at the beginning of the 21st century with their uncertainty ranges in parentheses.

	Wild et al. (2013)	JRA-25	JRA-55
Incoming solar	340 (340, 341)	341	341
Solar reflected	100 (96, 100)	95	100
Thermal outgoing	239 (236, 242)	255	251
Residual (downward)		–7.9	–10.0

Table 9. Global annual mean energy balance at the surface (W m^{-2}). Values from JRA-25 and JRA-55 are for the period 2002–2008, whereas those from Wild et al. (2013) represent present-day climate conditions at the beginning of the 21st century with their uncertainty ranges in parentheses.

	Wild et al. (2013)	JRA-25	JRA-55
Solar down	185 (179, 189)	197	189
Solar reflected	24 (22, 26)	25	26
Solar absorbed surface	161 (154, 166)	172	164
Solar absorbed atmosphere	79 (74, 91)	75	77
Residual (downward)	0.6 (0.2, 1.0)	–11.6	–11.2
Thermal down	342 (338, 348)	327	338
Thermal up	397 (394, 400)	399	400
Sensible heat	20 (15, 25)	20	20
Evaporation	85 (80, 90)	91	93

to the best estimate, due primarily to improvement of the clear-sky shortwave radiation scheme. In addition, revision of the reflectivity over deserts and the snow surface albedo over perennial land ice also increased the TOA reflected solar flux through increase of the surface reflected solar flux.

The incoming solar fluxes from JRA-25 and JRA-55 differ slightly from the best estimate of Wild et al. (2013). This is because the best estimate is based on the estimated solar irradiance (1360.8 ± 0.5 W m^{-2}) of Kopp et al. (2005) and Kopp and Lean (2011), whereas the previous estimate (1365 W m^{-2}, Kopp and Lean 2011) was used for JRA-25 and JRA-55.

Figure 18 shows the TOA radiation flux components from JRA-55 and their differences from the CERES-Energy Balanced and Filled (EBAF) flux dataset edition 2.7 (Loeb et al. 2009) and JRA-25. The TOA reflected solar fluxes of JRA-55 have generally increased from those of JRA-25, especially over the Amazon basin and desert/semidesert regions. Figure 19 shows the TOA cloud radiative effects (obtained from clear-sky and all-sky flux differences) from JRA-55 and their differences from CERES and JRA-25. The TOA solar flux reflected from clouds significantly increased over the Amazon basin in JRA-55 (Fig. 19c), which indicates that improved reproducibility of convective activities reduced negative biases in the TOA reflected solar fluxes over the region. An increase over desert and semidesert regions is due to revision of the albedo. Although this revision reduces negative biases over the Sahara, it exacerbates positive biases over other regions. It thus appears to be necessary to reevaluate the assumption of the same albedo for the Sahara and those regions. Moreover, there still remain positive biases over the tropics and subtropics, and negative biases over the Antarctic Ocean, which have been known since JRA-25 as pointed out by Trenberth and Smith (2008). The current shortwave radiation scheme assumes a random cloud overlap within the cloudy fraction of a model grid, which may lead to too much reflection of solar radiation over convective regions, where clouds tend to overlap maximally in the vertical (Kitagawa and Yabu 2002), which is most likely related to the positive biases over the tropics and subtropics.

For the outgoing thermal fluxes, a significant reduc-

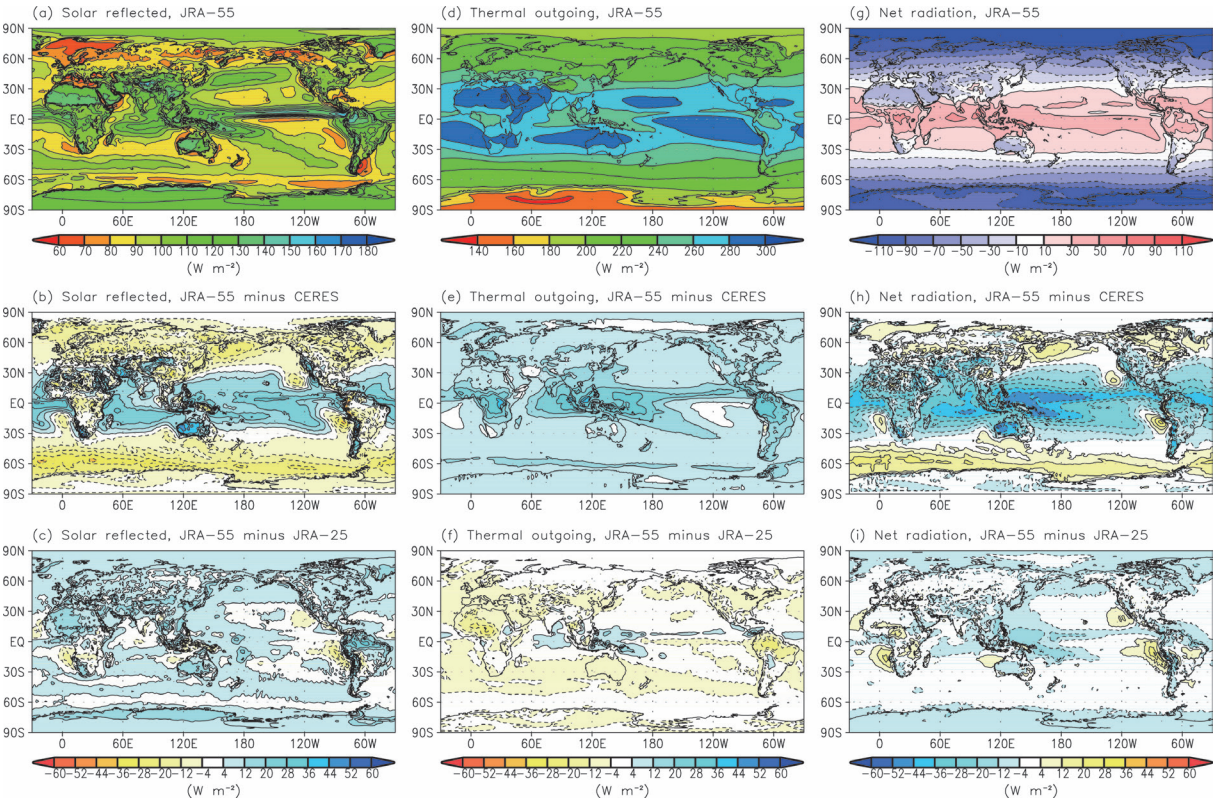

Fig. 18. (a–c) Reflected solar fluxes, (d–f) outgoing thermal fluxes, and (g–i) net radiation fluxes at the TOA from (a, d, g) JRA-55, and their differences from (b, e, h) CERES-EBAF ed. 2.7 and (c, f, i) JRA-25, averaged over 2002–2008.

tion of positive biases can be seen over the Amazon basin where a dry bias has been mitigated, most likely due to the increase of precipitable water. A modest reduction of positive biases can also be seen over most of the mid-latitudes. However, there still remain positive biases in deep convection regions over the tropics, particularly over the Indian Ocean, the western Pacific, the Intertropical Convergence Zone and the South Pacific Convergence Zone, where the biases become worse than JRA-25. This is most likely due to underestimation of cloud radiative effects in those regions (Figs 19e, f).

Because of the biases in the TOA reflected solar and outgoing thermal fluxes, the TOA net radiation fluxes from JRA-55 have too little absorption in the tropics and too little emission in the extratropics, a feature that has been seen since JRA-25. These biases may reduce activity in storm tracks and consequently reduce poleward energy transport (Trenberth and Fasullo 2010). Because these biases broadly correspond to the biases in the cloud radiative effects (Fig. 19), they are most likely related to representation of clouds (such as distribution, height and optical properties) and the cloud overlap assumptions made in the forecast model. There results clearly indicate the importance of improving representation of clouds for reproducing a more accurate energy balance.

8.2 Precipitation

It is crucially important to better understand mechanisms of each component of the hydrological cycle, such as precipitation, evaporation, atmospheric transport of water vapor, river runoff, for further advancing climate monitoring and climate modeling. Reanalysis can generate these variables as a synthesis of observations and modeling. However, forecast models have their own uncertainty, and corrections by observations introduce artificial source or sink into the water budget, which in turn leads to the spin-up (or spin-down) problem of the hydrological cycle. Also, changes in observing systems have a significant impact on the representation of hydrological cycle in

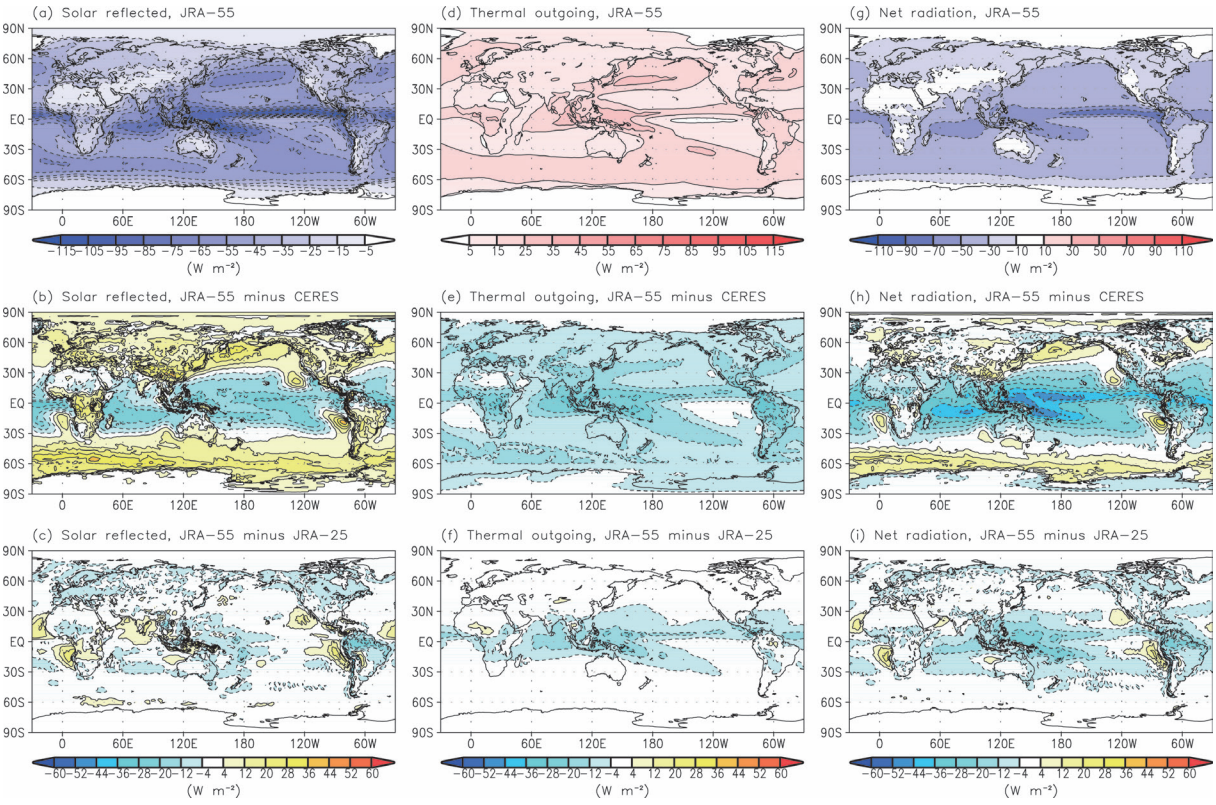

Fig. 19. Cloud radiative effects (obtained from clear-sky and all-sky flux differences) on (a–c) reflected solar fluxes, (d–f) outgoing thermal fluxes and (g–i) net radiation fluxes at the TOA from (a, d, g) JRA-55, and their differences from (b, e, h) CERES-EBAF ed. 2.7 and (c, f, i) JRA-25, averaged over 2002–2008.

reanalyses. Because of these weaknesses, it has been pointed out that great caution is needed when using hydrological variables from reanalyses, especially model diagnostics such as precipitation and evaporation (Bosilovich et al. 2011; Trenberth et al. 2011). Here, we examine main characteristics of the hydrological cycle in JRA-55 using GPCP V2.2 and other reanalyses, including JRA-25.

Figure 20 shows the climatology of global precipitation distributions in JRA-55, JRA-25, ERA-Interim, ERA-40, the Modern-Era Retrospective Analysis for Research and Applications (MERRA, Rienecker et al. 2011), and GPCP as an observational dataset. While precipitation in middle and high latitudes are underestimated in most reanalyses, this feature is improved in JRA-55, especially in the Pacific and Atlantic Oceans north of 30°N. On the other hand, JRA-55 overestimates precipitation in the tropics compared with GPCP. The regions where JRA-55 overestimates precipitation tend to exhibit the spin-down problem (precipitation is excessive immediately after the start of forecasts and then gradually decreases) (not shown). They also roughly correspond to the regions where large moistening increments occur (Fig. 11b). Therefore, the excessive precipitation in the tropics in JRA-55 is most likely related to the dry bias and the spin-down problem of the forecast model in regions of deep convection.

Figure 21 shows the time series of global monthly mean precipitation anomalies and their spatial anomaly correlation with GPCP. Although GPCP has no trend for the past 30 years, most of the reanalyses have strong trends, especially ERA-40 and MERRA. The time series from JRA-55 exhibits little trend and remains stable. The time series from the Twentieth Century Reanalysis (20CR, Compo et al. 2011) is even more stable, but its spatial anomaly correlations are not as high as the other latest generation reanalyses, most likely due to its sole reliance on surface pressure observations. Spatial anomaly correlations for JRA-55 are improved from JRA-25 by 0.1 throughout the study period, and exceed 0.6 after

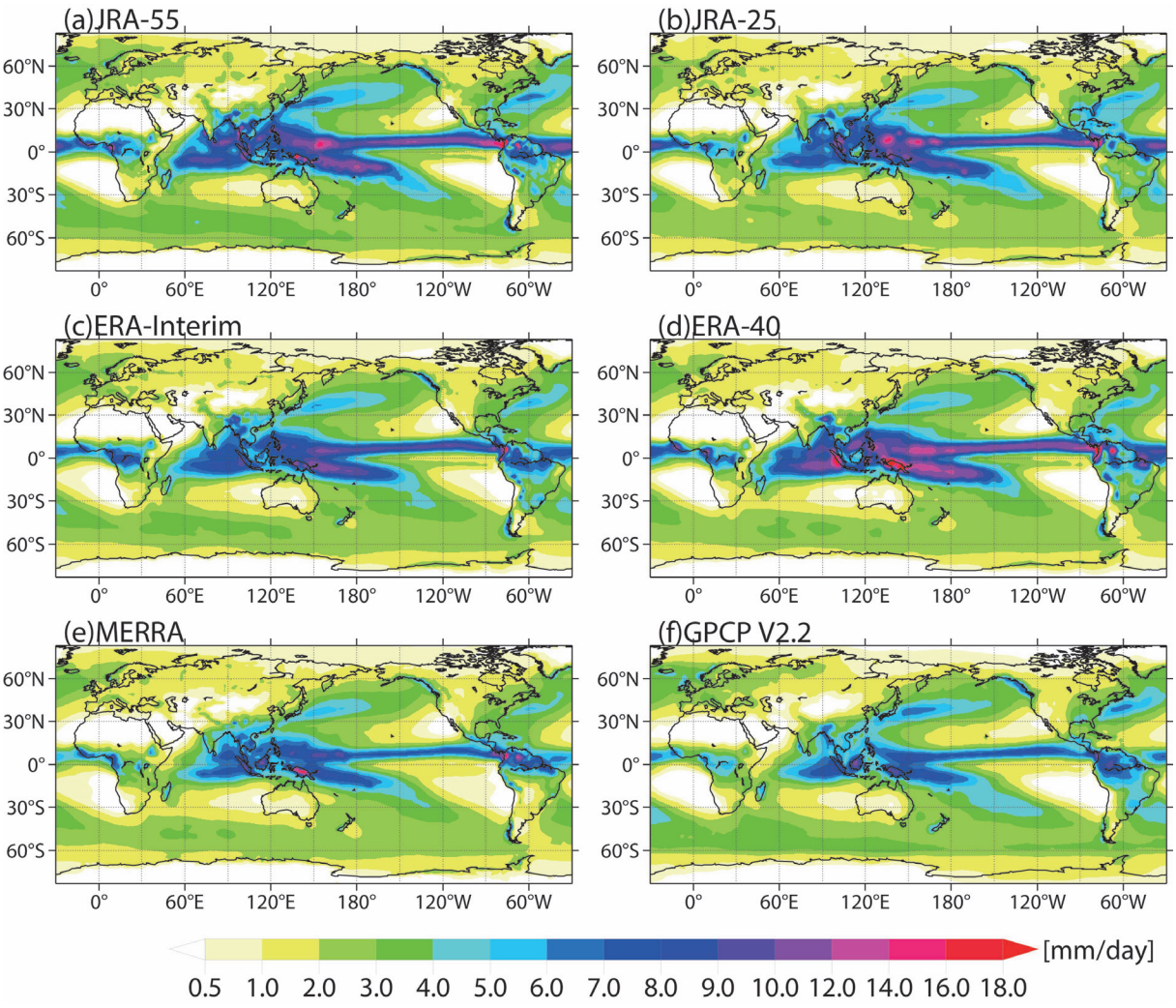

Fig. 20. Climatological annual mean precipitations in (a) JRA-55, (b) JRA-25, (c) ERA-Interim, (d) ERA-40, (e) MERRA, and (f) GPCP V2.2, averaged over 1980–2001.

the late 1980s (Fig. 21b). It should be noted that the abrupt increase in the late 1980s in most of the reanalyses is most likely due to the introduction of humidity observations from the SSM/I instrument on the Defense Meteorological Satellite Program satellites. Until then, spatial anomaly correlations for MERRA, ERA-Interim and the Climate Forecast System Reanalysis (CFSR, Saha et al. 2010) are higher than the others. Another important feature in Fig. 21b is the higher correlation in strong El Niño years, especially in 1997 and 1998 when the correlation was as high as 0.8. After the late 1990s, correlation coefficients for JRA-55, ERA-Interim and MERRA remained high at nearly 0.7, the highest among all reanalyses. The large increasing trend in spatial anomaly correlations for JRA-55 indicates that the reproducibility of precipitation has a great dependence on satellite observing systems compared with the other latest generation reanalyses, and suggests that there is a clear need for improving the reproducibility of precipitation, especially for the period before satellite observations increased substantially in the late 1990s.

8.3 Tropical cyclones

In JRA-25, TCRs were assimilated for the first time in reanalyses, contributing to a better representation of tropical cyclones than other reanalyses of the time (Hatsushika et al. 2006). However, the TCRs used

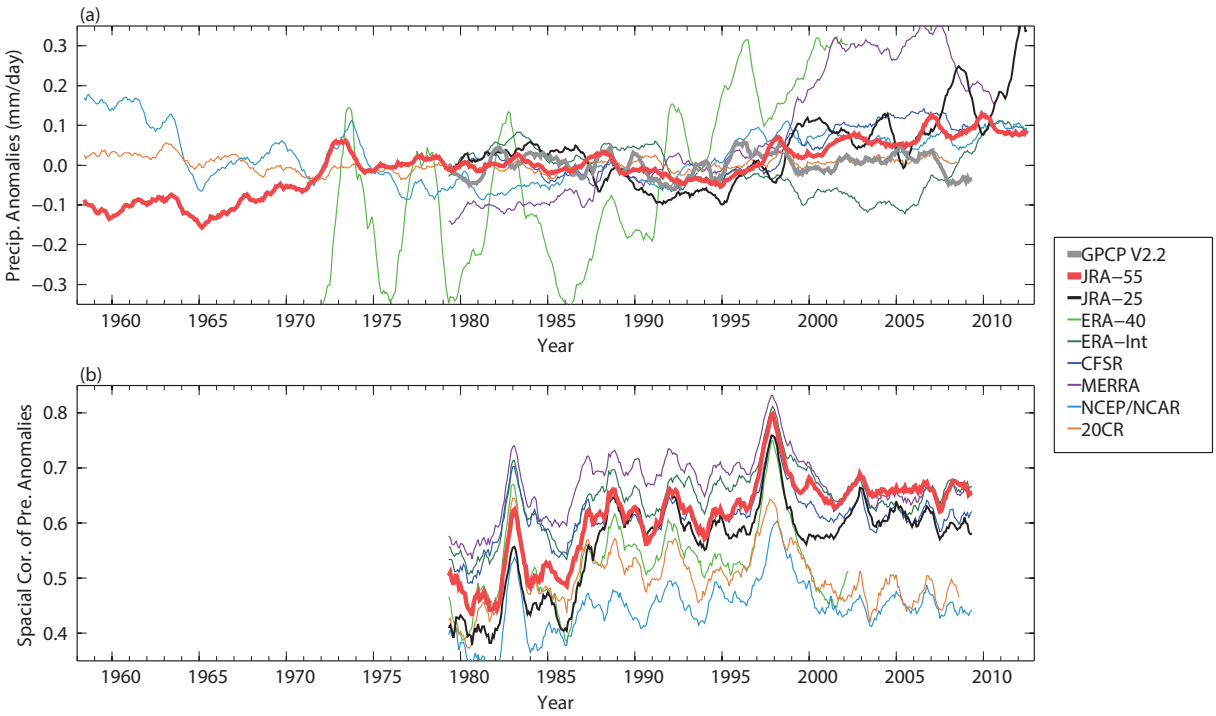

Fig. 21. (a) Global monthly mean precipitation anomalies from reanalyses and GPCP V2.2, and (b) 12-month running mean spatial anomaly correlations against GPCP V2.2. Anomalies for each dataset were defined relative to their own climatological monthly means over 1980–2001.

in JRA-25 contained some duplications and location errors that originated in best-track data; accordingly, for JRA-55 the TCRs were regenerated with improved QC for best-track data.

Figure 22 shows global detection rates of tropical cyclones in JRA-55, JRA-25, and ERA-Interim. The observational definition of a tropical cyclone is a tropical disturbance with maximum sustained wind speed of 34 knots (17.5 m s^{-1}) or greater, but this criterion is not applicable to grid point data. Instead, the detection criterion for isobaric fields by Hatsushika et al. (2006) was employed. Horizontal resolutions of the grid point data used in this study are 1.25° in JRA-55 and JRA-25 and 1.5° in ERA-Interim, but the same detection criterion was applied for them because the difference did not significantly affect the result. The detection rate in JRA-55 is around 95 % from the 1950s to the 1980s, after which it gradually decreases to 85–90 % in the 2000s, while the detection rate in JRA-25 is almost constant at 90 % except during the late 2000s (Fig. 22). As shown in Figs. 2, 3 and 4, the number of observations increases with time, particularly satellite data, which should lead to increasing

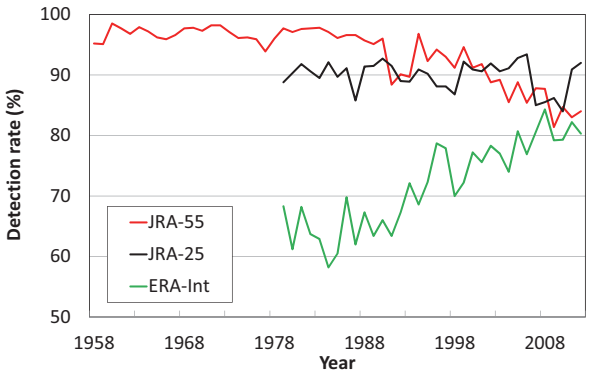

Fig. 22. Global detection rates of tropical cyclones in JRA-55, JRA-25, and ERA-Interim.

detection rates with time. In ERA-Interim, the detection rate increases from 60 % in the 1980s to 75–80 % in the 2000s.

Figure 23 shows the global mean maximum 10 m wind speed of tropical cyclones detected in JRA-55, JRA-25, and ERA-Interim. A weakening trend is

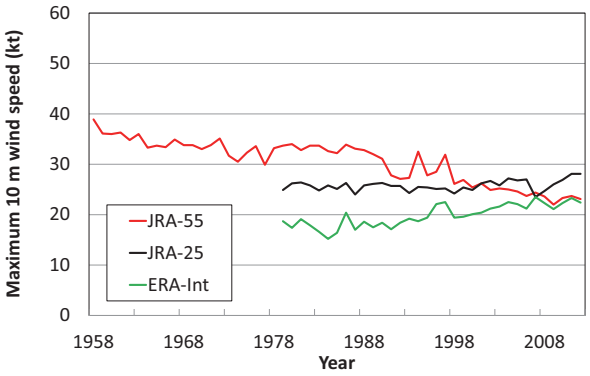

Fig. 23. Global mean maximum 10 m wind speeds around detected tropical cyclone center in JRA-55, JRA-25, and ERA-Interim.

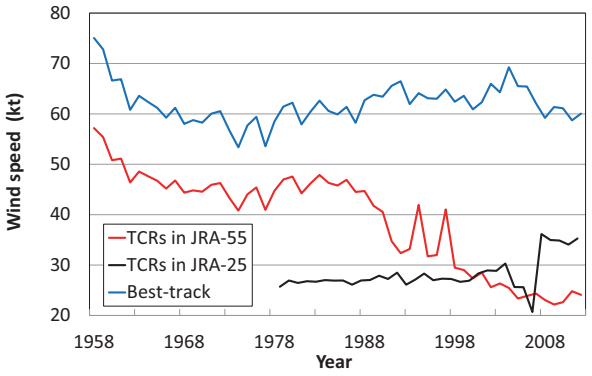

Fig. 24. Global mean wind speed of the TCRs assimilated in JRA-55 and JRA-25, and maximum sustained wind speed reported in the best–track data.

evident in JRA-55 with maximum 10 m wind speeds decreasing from around 35 kt in the 1960s to 25 kt in the 2000s. On the other hand, JRA-25 shows no trend in the mean wind speed of tropical cyclones. For ERA-Interim, in which no artificial tropical cyclone information like TCRs is assimilated, it is reasonable that the increasing trend in wind speed leads to an increasing trend in the detection rate. The intensifying trend of tropical cyclones in ERA-Interim directly reflects increasing observations and improving representation of tropical cyclones. The weakening trend of tropical cyclones in JRA-55 goes against the effect of increasing observations.

Figure 24 shows the global mean annual wind speeds of TCRs assimilated in JRA-55 and JRA-25, together with the maximum sustained wind speeds from best-track data for reference. For JRA-55, these have almost constant values of 40–50 kt with no trend from the 1960s to the 1980s and are consistent with the best-track data, after which they decrease to around 20–25 kt in the 2000s, which is inconsistent with the best-track data. On the other hand, the global mean annual wind speeds of TCRs assimilated in JRA-25 were almost constant around 25 kt except in the late 2000s, resulting in constant detection rates throughout the study period.

The TCRs were retrieved from position, maximum sustained wind speed, radius of 30-kt winds (R30) and 12-hour motion. Figure 25 shows the annual variation in the existing rates of R30 in the best-track data. Since the R30 records were only available after the late 1980s, R30s were taken from a look-up table in JRA-25 instead. In JRA-55, on the other hand, R30s were taken not from the look-up table but from the

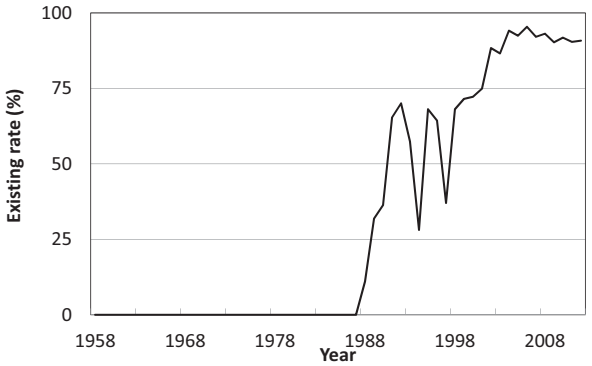

Fig. 25. Existing rates of the R30 in the best-track data.

best-track data. When the R30 record was not available, a predefined fixed value was used for R30. However, there is a considerable difference between the predefined fixed value and R30s in the best-track data; consequently, TCR speeds vary significantly depending on whether the R30 record is available or not. Comparing Figs. 24 and 25, a negative correlation is evident between TCR speed in JRA-55 and availability of R30 records.

Although TCRs assimilated in JRA-55 show the artificial weakening trend, they are still useful for representing tropical cyclones in the correct locations, which can be confirmed by the fact that high detection rates are maintained in JRA-55. Thus, JRA-55 can provide a proper dataset for a case study of an individual tropical cyclone. However, the trend of

tropical cyclone frequency and intensity in JRA-55 is most likely affected by the artificial weakening trend of TCRs. Further examination is currently underway to assess the impact of the artificial weakening trend of TCRs on the representation of tropical cyclones in JRA-55.

9. Conclusions

JRA-55 has been produced with the low-resolution (TL319) version of JMA's operational data assimilation system as of December 2009, which incorporated many improvements that had been achieved since JRA-25, including the revised longwave radiation scheme, 4D-Var and VarBC for satellite radiances. In addition, newly available homogenized observations were used in JRA-55 whenever possible. These improvements have resulted in products that produce better fits to observations, reduced analysis increments and improved forecast scores. These are evidence of the greater physical consistency of the JRA-55 product.

A cold bias in the lower stratosphere, one of the major problems of JRA-25, has been diminished owing primarily to the proper representation of absorptions due to the Doppler broadening in the revised longwave radiation scheme. The surface downward thermal flux has drawn closer to the observational best estimate, most likely due to the improved representation of water vapor continuum absorption in longwave radiation. The temporal consistency of temperature analysis has improved considerably from previous reanalyses, thanks to improved model climatology, newly available bias estimates to homogenize radiosonde temperatures and advances in handling satellite radiances. A dry bias in the Amazon basin, another major problem of JRA-25, has been mitigated temporarily by excluding surface pressure observations over the Amazon basin. However, more work is needed to solve this problem.

Our initial quality evaluation has revealed problems such as a warm bias in the upper troposphere, a cold bias in the lower troposphere and a negative bias in precipitable waters in deep convection regions. The warm bias in the upper troposphere gradually decreases as the observing system is improved. The impact of changes in observing systems is particularly apparent in July 2006 when the GNSS-RO refractivities were introduced into JRA-55. In order to improve the temporal consistency of product, these model biases must be further reduced. Some of the diagnostic fields from the forecast model still exhibit large biases, e.g., excessive precipitation over the tropics, excessive (insufficient) TOA reflected solar flux over the tropics and subtropics (the Antarctic Ocean), excessive outgoing thermal flux in deep convection regions, and an overall imbalance of 10 W m^{-2} upward in the global mean net energy fluxes at the TOA and the surface. For these diagnostic fields to be useful in climate applications, the parameterizations of physical processes must be further improved. Our work also showed that tropical cyclone strength analyzed in JRA-55 has unrealistic trends. This has most likely stemmed from the retrieval method for TCR, which highlights anew the importance of homogeneity of observations in reanalysis.

To aid further study of the reproducibilities of low-frequency variability and trends in JRA-55, as well as the impacts of model biases and changes of observing systems, MRI has produced a reanalysis assimilating conventional observations only, called JRA-55C (Kobayashi et al. 2014), and an Atmospheric Model Intercomparison Project (AMIP)-type simulation, called JRA-55AMIP. These are produced with the same NWP system as the one used for JRA-55, and they are made available together with JRA-55 products as the JRA-55 family. Intercomparisons among the JRA-55 family are expected to contribute to spotting problems in the data assimilation system and forecast model that can lead to improvement of future reanalyses.

The high-resolution ocean surface boundary condition is also worth consideration for future reanalyses. Nakamura et al. (2008) suggested the importance of mid-latitude oceanic fronts for the tropospheric circulation and its variability. The representation of mid-latitude oceanic fronts in COBE-SST, which was used for JRA-55, is insufficiently accurate due to its moderate resolution (1° × 1°) and its sole reliance on in-situ observations. For the period during which satellite observations are available, the use of high-resolution SST using all available satellite data needs to be explored.

It is essential to improve quality and availability of observational datasets for further advances in reanalysis. Several international activities are retrieving historical observations and reprocessing satellite observations, such as European Reanalysis of Global Climate Observations (ERA-CLIM, http://www.era-clim.eu/) and SCOPE-CM. Observational datasets to be made available through these activities are indispensable for improving reanalyses.

Acknowledgments

The JRA-55 project was conducted in cooperation

with many divisions of JMA. The data assimilation system used for JRA-55 is an achievement of many years of development at the Numerical Prediction Division. MSC reprocessed AMVs and CSRs from past GMS and MTSAT imagery. The three-dimensional daily ozone distributions were produced in cooperation with the Atmospheric Environment Division. In addition, many individuals from the Climate Prediction Division and MRI contributed to quality evaluation of the product from the start of the production of JRA-55.

JRA-55 is also supported by many individuals and organizations in collecting observations. The JRA-55 observational dataset consists primarily of the ERA-40 observational dataset which was supplied by ECMWF. Dr. Michael Fiorino of NOAA regenerated TCRs, and also provided us with the software for generating them on a near real-time basis. Furthermore, various kinds of observations were supplied by organizations listed in Appendix A.

Satellite radiances were assimilated with RTTOV-9.3 which was developed within the European Organisation for the Exploitation of Meteorological Satellites (EUMETSAT) Satellite Application Facility on Numerical Weather Prediction (NWP SAF). Dr. Roger Saunders of the Met Office supplied us with the latest radiative transfer coefficients for VTPR and GMS-5.

The JRA-55 advisory committee, with Prof. Toshiki Iwasaki of Tohoku University as chairman, provided us with valuable advice on broad aspects of reanalysis from the outset of the project. In addition, 27 external researchers participated in quality evaluation prior to release of the product.

The JRA-55 project was realized with support from these individuals and organizations. We sincerely appreciate their invaluable contributions.

Appendix A: Observational data sources for JRA-55

The suppliers of observations used in JRA-55, the type of data and the period for which the data were used are given in Table A1.

Appendix B: Acronyms

1D-Var	One-dimensional variational analysis
20C3M	Twentieth century climate in coupled models
20CR	Twentieth Century Reanalysis
2D-OI	Two-dimensional OI
3D-Var	Three-dimensional variational analysis
4D-Var	Four-dimensional variational analysis
AMI	Active Microwave Instrument
AMIP	Atmospheric Model Intercomparison Project
AMSR-E	Advanced Microwave Scanning Radiometer for EOS
AMSU	Advanced Microwave Sounding Unit
AMV	Atmospheric motion vector
ASCAT	Advanced Scatterometer
ASPS	Advanced Scatterometer Processing System
ATOVS	Advanced TOVS
BFGS	Broyden-Fletcher-Goldfarb-Shanno (algorithm)
BSRN	Baseline Surface Radiation Network
BUOY	Report of a buoy observation
C/NOFS	Communications/Navigation Outage Forecasting System
CAPE	Convective available potential energy
CCM	Chemistry climate model
CDAAC	COSMIC Data Analysis and Archive Center
CERES	Clouds and the Earth's Radiant Energy System
CFSR	Climate Forecast System Reanalysis
CHAMP	Challenging Mini-satellite Payload
CLASS	Comprehensive Large Array-data Stewardship System
CMIP5	Coupled Model Intercomparison Project Phase 5
CMOD	C-band model function
COBE	Centennial In Situ Observation-based Estimates of the Variability of SSTs and Marine Meteorological Variables
COSMIC	Constellation Observing System for Meteorology, Ionosphere, and Climate
CRIEPI	Central Research Institute of Electric Power Industry
CRU	Climatic Research Unit
CRUTEM4	CRU temperature dataset
CSR	Clear sky radiance
DCAPE	Dynamic CAPE generation rate
DOE	Department of Energy
EBAF	Energy Balanced and Filled (flux dataset)
ECMWF	European Centre for Medium-Range Weather Forecast
EORC	Earth Observation Research Center
EOS	Earth Observing System (NASA)
ERA	ECMWF Reanalysis
ERA-40	A 45-year ERA from September 1957 to August 2002
ERA-CLIM	European Reanalysis of Global Climate Observations

Table A1. Observational data sources for JRA-55. Observations shown in plain cells were added or reprocessed after JRA-25, whereas those in shaded cells are the same as the ones used in JRA-25.

Data supplier	Data type and suppliers' identifiers	Period	Note
Conventional data			
ECMWF		Jan 1958–Aug 2002	Uppala et al. (2005)
JMA		Jan 1961–	
	GAME and SCSMEX	Apr 1998–Oct 1998	
NCEP/NCAR	SYNOP and upper-level observations	Jan 1979–Dec 1979	Kalnay et al. (1996) Kistler et al. (2001)
M. Yamanaka	Radiosondes from Indonesia	Nov 1991–May 1999	Okamoto et al. (2003)
M. Fiorino	TCRs	Jan 1958–	Fiorino (2002)
RIHMI	Snow depths from Russia	Jan 1958–Dec 2008	http://meteo.ru/english/climate/snow.php
UCAR	Snow depths from USA	Jan 1958–Aug 2011	NCDC et al. (1981)
Monthly Surface Meteorological Data in China	Snow depths from China	Jan 1971–Dec 2006	Digitized from printed matters
IMH	Snow depths from Mongolia	Jan 1975–Dec 2007	
Satellite radiances			
ECMWF	VTPR	Jan 1973–Feb 1979	Uppala et al. (2005)
	HIRS and SSU	Nov 1978–Dec 2000	
	MSU and AMSU	Nov 1978–May 2003	
NOAA/NCDC	SSM/I	Jun 1987–Dec 2004	
NOAA/CLASS	AMSU and MHS	Aug 1998–	
	SSM/I	Jul 1987–	
JMA	AMSU and MHS	Jun 2003–	
	SSM/I and SSMIS	Mar 2006–	
	TMI	Dec 2011–	
	CSR	Jun 2005–	
JMA/MSC	Reprocessed CSRs from GMS-5, GOES 9 and MTSAT-1R	Jul 1995–Dec 2009	
JAXA, NASA	Reprocessed TMI Version 7	Feb 1998–Dec 2011	
JAXA	Reprocessed AMSR-E Version 3	Jun 2002–Oct 2011	
EUMETSAT	CSRs from the Meteosat series	Jan 2001–Aug 2009	
AMVs			
ECMWF	GMS, Meteosat and GOES	Jan 1979–Dec 1997	Uppala et al. (2005)
JMA	GMS, MTSAT, Meteosat and GOES	Dec 1979–Dec 1980 Jan 1998–	
	MODIS	Jun 2004–	
JMA/MSC	Reprocessed GMS, GOES 9 and MTSAT-1R	Jan 1979–Nov 1979 Mar 1987–Sep 2009	
EUMETSAT	Reprocessed Meteosat-2	May 1982–Aug 1988	van de Berg et al. (2002)
	Reprocessed Meteosat-3 to -7	Jan 1989–Dec 2000 Aug 1988–Nov 1988	
	Meteosat-5 and -7	Jan 2001–Feb 2001	
Scatterometer ocean surface winds			
ESA	Reprocessed AMI (ERS.ASPS20.N)	May 1997–Jan 2001	De Chiara et al. (2007)
Hersbach (2008)			
JPL	Reprocessed SeaWinds from QuikSCAT (QSCAT_LEVEL_2B_V2)	Jul 1999–Nov 2009	Dunbar et al. (2006)
JMA	ASCAT	Jan 2008–	
GNSS-RO refractivities			
CDAAC	Reprocessed CHAMP, SAC-C, COSMIC, GRACE, Metop-A, TerraSAR-X and C/NOFS	Jul 2006–Jun 2012	
JMA	COSMIC, GRACE, Metop, TerraSAR-X and C/NOFS	Jun 2012–	

ERS	European Remote Sensing Satellite
ESA	European Space Agency
EUMETSAT	European Organisation for the Exploitation of Meteorological Satellites
FAA	Federal Aviation Administration
FGAT	First guess at the appropriate time
FGGE	First GARP Global Experiment
FOV	Field of view
GAME	GEWEX Asia Monsoon Experiment
GARP	Global Atmospheric Research Programme
GEBA	Global energy balance archive
GEWEX	Global Energy and Water Cycle Experiment
GMS	Geostationary Meteorological Satellite
GNSS-RO	Global Navigation Satellite System–Radio Occultation
GOES	Geostationary Operational Environmental Satellite
GPCC	Global Precipitation Climatology Centre
GPCP	Global Precipitation Climatology Project
GRACE	Gravity Recovery and Climate Experiment
GSM	Global spectral model
HadAT	Hadley Centre's radiosonde temperature product
HIRS	High-Resolution Infrared Spectrometer
HITRAN	High Resolution Transmission
IMH	Institute of Meteorology and Hydrology (Mongolia)
JAXA	Japan Aerospace Exploration Agency
JCDAS	JMA Climate Data Assimilation System
JMA	Japan Meteorological Agency
JPL	Jet Propulsion Laboratory
JRA-25	Japanese 25-year Reanalysis
JRA-55	Japanese 55-year Reanalysis
JRA-55AMIP	JRA-55 AMIP-type simulation
JRA-55C	JRA-55 sub-product assimilating Conventional observations only
LBLRTM	Line-by-Line Radiative Transfer Model
MERRA	Modern-Era Retrospective Analysis for Research and Applications
MHS	Microwave Humidity Sounder
MODIS	Moderate Resolution Imaging Spectroradiometer
MRI	Meteorological Research Institute (JMA)
MSC	Meteorological Satellite Center (JMA)
MSG	Meteosat Second Generation
MSU	Microwave Sounding Unit
MT_CKD	Mlawer–Tobin–Clough–Kneizys–Davies (water vapor continuum absorption model)
MTSAT	Multi-functional Transport Satellite
NASA	National Aeronautics and Space Administration
NCAR	National Center for Atmospheric Research
NCDC	National Climate Data Center
NCEP	National Center for Environmental Prediction
NOAA	National Oceanic and Atmospheric Administration
NWP	Numerical weather prediction
NWP SAF	Satellite Application Facility on Numerical Weather Prediction
NWS	National Weather Service
OI	Optimal interpolation
OMI	Ozone Monitoring Instrument
PAOBS	Pseudo Surface Pressure Observations produced by Australia
QC	Quality control
QuikSCAT	Quick Scatterometer
R30	Radius of 30-kt winds
RAOBCORE	Radiosonde Observation Correction using Reanalyses
RCP	Representative Concentration Pathway
RIHMI	Russian Research Institute for Hydrometeorological Information
RMS	Root-mean-square
RSS	Remote Sensing Systems
RTTOV	Radiative Transfer for the TIROS Operational Vertical Sounder
SAC-C	Satélite de Aplicaciones Cientificas-C
SCOPE-CM	Sustained, Coordinated Processing of Environmental Satellite Data for Climate Monitoring
SCSMEX	South China Sea Monsoon Experiment
SEVIRI	Spinning Enhanced Visible and Infrared Imager
SHIP	Report of surface observation from a sea station
SiB	Simple Biosphere (model)
SMS	Supervisor Monitor Scheduler
SSM/I	Special Sensor Microwave/Imager
SSMIS	Special Sensor Microwave Imager Sounder
SST	Sea surface temperature

SSU	Stratospheric Sounding Unit
STAR	Center for Satellite Applications and Research
SYNOP	Report of surface observation from a fixed land station
TCR	Wind profile retrieval surrounding tropical cyclones
TIROS	Television and Infrared Observation Satellite
TMI	TRMM Microwave Imager
TOA	Top of the atmosphere
TOMS	Total Ozone Mapping Spectrometer
TOVS	TIROS Operational Vertical Sounder
TRMM	Tropical Rainfall Measurement Mission
UCAR	University Corporation for Atmospheric Research
VarBC	Variational bias correction
VTPR	Vertical Temperature Profile Radiometer
WDCGG	World Data Centre for Greenhouse Gases
WMO	World Meteorological Organization

References

Adler, R. F., G. J. Huffman, A. Chang, R. Ferraro, P.-P. Xie, J. Janowiak, B. Rudolf, U. Schneider, S. Curtis, D. Bolvin, A. Gruber, J. Susskind, P. Arkin, and E. Nelkin, 2003: The Version-2 Global Precipitation Climatology Project (GPCP) monthly precipitation analysis (1979-present). *J. Hydrometeor.*, **4**, 1147–1167.

Andrae, U., N. Sokka, and K. Onogi, 2004: *The radiosonde temperature bias corrections used in ERA-40.* ECMWF ERA-40 Project Report Series, **15**, ECMWF, UK, 34 pp. [Available at http://www.ecmwf.int/en/research/publications/.]

Arakawa, A., and W. H. Schubert, 1974: Interaction of a cumulus cloud ensemble with the large-scale environment, Part I. *J. Atmos. Sci.*, **31**, 674–701.

Arking, A., and K. Grossman, 1972: The influence of line shape and band structure on temperatures in planetary atmospheres. *J. Atmos. Sci.*, **29**, 937–949.

Bengtsson, L., P. Arkin, P. Berrisford, P. Bougeault, C. K. Folland, C. Gordon, K. Haines, K. I. Hodges, P. Jones, P. Kallberg, N. Rayner, A. J. Simmons, D. Stammer, P. W. Thorne, S. Uppala, and R. S. Vose, 2007: The need for a dynamical climate reanalysis. *Bull. Amer. Meteor. Soc.*, **88**, 495–501.

Bosilovich, M. G., F. R. Robertson, and J. Chen, 2011: Global energy and water budgets in MERRA. *J. Climate*, **24**, 5721–5739.

Bréon, F.-M., D. Jackson, and J. Bates, 1999: Evidence of atmospheric contamination on the measurement of the spectral response of the GMS-5 water vapor channel. *J. Atmos. Oceanic Technol.*, **16**, 1851–1853.

Briegleb, B. P., 1992: Delta-Eddington approximation for solar radiation in the NCAR community climate model. *J. Geophys. Res.*, **97**, 7603–7612.

Briegleb, B. P., P. Minnis, V. Ramanathan, and E. Harrison, 1986: Comparison of regional clear-sky albedos inferred from satellite observations and model computations. *J. Climate Appl. Meteor.*, **25**, 214–226.

Chou, M.-D., and L. Kouvaris, 1991: Calculations of transmission functions in the infrared CO_2 and O_3 bands. *J. Geophys. Res.*, **96**, 9003–9012.

Chou, M.-D., M. J. Suarez, X.-Z. Liang, and M. M.-H. Yan, 2001: *A thermal infrared radiation parameterization for atmospheric studies.* Technical report series on global modeling and data assimilation, NASA/TM-2001-104606, 19, National Aeronautics and Space Administration (NASA) Goddard Space Flight Center, USA, 68 pp. [Available at http://ntrs.nasa.gov/.]

Clarke, L., J. Edmonds, H. Jacopy, H. Pitcher, J. Reilly, and R. Richels, 2007: *Scenarios of greenhouse gas emissions and atmospheric concentrations.* Sub-report 2.1A of Synthesis and Assessment Product 2.1 by the U.S. Climate Change Science Program and the Subcommittee on Global Change Research. Department of Energy (DOE), Office of Biological & Environmental Research, USA, 154 pp. [Available at http://library.globalchange.gov/products.]

Clough, S. A., and M. J. Iacono, 1995: Line-by-line calculation of atmospheric fluxes and cooling rates 2. Application to carbon dioxide, ozone, methane, nitrous oxide and the halocarbons. *J. Geophys. Res.*, **100**, 16519–16535.

Clough, S. A., M. J. Iacono, and J.-L. Moncet, 1992: Line-by-line calculations of atmospheric fluxes and cooling rates: Application to water vapor. *J. Geophys. Res.*, **97**, 15761–15785.

Clough, S. A., M. W. Shephard, E. J. Mlawer, J. S. Delamere, M. J. Iacono, K. Cady-Pereira, S. Boukabara, and P. D. Brown, 2005: Atmospheric radiative transfer modeling: a summary of the AER codes. *J. Quant. Spectrosc. Radiat. Transfer*, **91**, 233–244.

Coakley, J. A., Jr., R. D. Cess, and F. B. Yurevich, 1983: The effect of tropospheric aerosols on the earth's radiation budget: a parameterization for climate models. *J. Atmos. Sci.*, **40**, 116–138.

Compo, G. P., J. S. Whitaker, P. D. Sardeshmukh, N. Matsui, R. J. Allan, X. Yin, B. E. Gleason, R. S. Vose, G. Rutledge, P. Bessemoulin, S. Brönnimann, M. Brunet, R. I. Crouthamel, A. N. Grant, P. Y. Groisman, P. D. Jones, M. C. Kruk, A. C. Kruger, G. J. Marshall, M. Maugeri, H. Y. Mok, Ø. Nordli, T. F. Ross, R. M. Trigo, X. L. Wang, S. D. Woodruff, and S. J. Worley, 2011. The Twentieth Century Reanalysis Project. *Quart. J. Roy. Meteor. Soc.*, **137**, 1–28.

Courtier, P., J.-N. Thépaut, and A. Hollingsworth, 1994: A strategy for operational implementation of 4D-Var, using an incremental approach. *Quart. J. Roy. Meteor. Soc.*, **120**, 1367–1387.

De Chiara, G., R. Crapolicchio, and P. Lecomte, 2007: *ERS-1/2 scatterometer new products: mission reprocessing and data quality improvement.* Paper presented at the 2nd Space for Hydrology Workshop, Geneva, Switzerland, November 12-14, 2007. [Available at http://earth.esa.int/hydrospace07/programme.html.]

Dee, D. P., and S. Uppala, 2009: Variational bias correction of satellite radiance data in the ERA-Interim reanalysis. *Quart. J. Roy. Meteor. Soc.*, **135**, 1830–1841.

Dee, D. P., S. M. Uppala, A. J. Simmons, P. Berrisford, P. Poli, S. Kobayashi, U. Andrae, M. A. Balmaseda, G. Balsamo, P. Bauer, P. Bechtold, A. C. M. Beljaars, L. van de Berg, J. Bidlot, N. Bormann, C. Delsol, R. Dragani, M. Fuentes, A. J. Geer, L. Haimberger, S. B. Healy, H. Hersbach, E. V. Hólm, L. Isaksen, P. Kållberg, M. Köhler, M. Matricardi, A. P. McNally, B. M. Monge-Sanz, J.-J. Morcrette, B.-K. Park, C. Peubey, P. de Rosnay, C. Tavolato, J.-N. Thépaut, and F. Vitart, 2011: The ERA-Interim reanalysis: configuration and performance of the data assimilation system. *Quart. J. Roy. Meteor. Soc.*, **137**, 553–597.

Derber, J., and F. Bouttier, 1999: A reformulation of the background error covariance in the ECMWF global data assimilation system. *Tellus A*, **51**, 195–221.

Derber, J. C., and W.-S. Wu, 1998: The use of TOVS cloud-cleared radiances in the NCEP SSI analysis system. *Mon. Wea. Rev.*, **126**, 2287–2299.

Desroziers, G., L. Berre, B. Chapnik, and P. Poli, 2005: Diagnosis of observation, background and analysis error statistics in observation space. *Quart. J. Roy. Meteor. Soc.*, **131**, 3385–3396.

Dorman, J. L., and P. J. Sellers, 1989: A global climatology of albedo, roughness length and stomatal resistance for atmospheric general circulation models as represented by the Simple Biosphere Model (SiB). *J. Appl. Meteor.*, **28**, 833–855.

Dunbar, R. S., T. Lungu, B. Weiss, B. Stiles, J. Huddleston, P. S. Callahan, G. Shirtliffe, K. L. Perry, C. Hsu, C. Mears, F. Wentz, and D. Smith, 2006: *QuikSCAT science data product user's manual.* Version 3.0, D-18053 - Rev A, Jet Propulsion Laboratory (JPL), USA, 85 pp.

Ebert, E. E., and J. A. Curry, 1992: A parameterization of ice cloud optical properties for climate models. *J. Geophys. Res.*, **97**, 3831–3836.

Ebita, A., S. Kobayashi, Y. Ota, M. Moriya, R. Kumabe, K. Onogi, Y. Harada, S. Yasui, K. Miyaoka, K. Takahashi, H. Kamahori, C. Kobayashi, H. Endo, M. Soma, Y. Oikawa, and T. Ishimizu, 2011: The Japanese 55-year Reanalysis "JRA-55": an interim report. *SOLA*, **7**, 149–152.

Etheridge, D. M, L. P. Steele, R. L. Langenfelds, R. J. Francey, J.-M. Barnola, and V. I. Morgan, 1998: Historical CO_2 records from the Law Dome DE08, DE08-2, and DSS ice cores. *Trends: A Compendium of Data on Global Change*. Carbon Dioxide Information Analysis Center, Oak Ridge National Laboratory, DOE, USA. [Available at http://cdiac.ornl.gov/trends/co2/lawdome.html.]

Fiorino, M., 2002: Analysis and forecasts of tropical cyclones in the ECMWF 40-year reanalysis (ERA-40). *25th Conference on Hurricanes and Tropical Meteorology*, CA, USA, 261–264.

Freidenreich, S. M., and V. Ramaswamy, 1999: A new multiple-band solar radiative parameterization for general circulation models. *J. Geophys. Res.*, **104**, 31389–31409.

Geleyn, J.-F., and A. Hollingsworth, 1979: An economical analytical method for the computation of the interaction between scattering and line absorption of radiation. *Beitr. Phys. Atmos.*, **52**, 1–16.

Goody, R. M., 1952: A statistical model for water-vapour absorption. *Quart. J. Roy. Meteor. Soc.*, **78**, 165–169.

Haimberger, L., C. Tavolato, and S. Sperka, 2008: Toward elimination of the warm bias in historic radiosonde temperature records--Some new results from a comprehensive intercomparison of upper-air data. *J. Climate*, **21**, 4587–4606.

Haimberger, L., C. Tavolato, and S. Sperka, 2012: Homogenization of the global radiosonde temperature dataset through combined comparison with reanalysis background series and neighboring stations. *J. Climate*, **25**, 8108–8131.

Hatsushika, H., J. Tsutsui, M. Fiorino, and K. Onogi, 2006: Impact of wind profile retrievals on the analysis of tropical cyclones in the JRA-25 reanalysis. *J. Meteor. Soc. Japan*, **84**, 891–905.

Hersbach, H., 2008: *CMOD5.N: A C-band geophysical model function for equivalent neutral wind.* ECMWF Technical Memorandom, **554**, ECMWF, UK, 20 pp. [Available at http://www.ecmwf.int/en/research/publications/.]

Holmlund, K., 1998: The utilization of statistical properties of satellite-derived atmospheric motion vectors to derive quality indicators. *Wea. Forecasting*, **13**, 1093–1104.

Ishibashi, T., 2009: Assimilation of WV-CSRs from five geostationary satellites in the JMA global 4D-Var system. *CAS/JSC WGNE Res. Activ. Atmos. Oceanic Modell.*, **39**, 13–14. [Available at http://www.wcrp-climate.org/WGNE/blue_book.html.]

Ishii, M., A. Shouji, S. Sugimoto, and T. Matsumoto, 2005: Objective analyses of sea-surface temperature and marine meteorological variables for the 20th century using ICOADS and the KOBE collection. *Int. J. Climatol.*, **25**, 865–879.

Iwamura, K., and H. Kitagawa, 2008: An upgrade of the

JMA operational global NWP model. *CAS/JSC WGNE Res. Activ. Atmos. Oceanic Modell.*, **38**, 3–4. [Available at http://www.wcrp-climate.org/WGNE/blue_book.html.]

JMA, 2002: Outline of the operational numerical weather prediction at the Japan Meteorological Agency. *WMO Numerical Weather Prediction Progress Report*. JMA, Japan, 158 pp.

JMA, 2007: Outline of the operational numerical weather prediction at the Japan Meteorological Agency. *WMO Technical Progress Report on the Global Data-Processing and Forecasting System and Numerical Weather Prediction*, JMA, Japan, 194 pp. [Available at http://www.jma.go.jp/jma/jma-eng/jma-center/nwp/nwp-top.htm.]

JMA, 2013a: *JRA-55 product users' handbook: 1.25 degree latitude/longitude grid data*. JMA, Japan, 22 pp. [Available at http://jra.kishou.go.jp/JRA-55/index_en.html.]

JMA, 2013b: Outline of the operational numerical weather prediction at the Japan Meteorological Agency. *WMO Technical Progress Report on the Global Data-processing and Forecasting System (GDPFS) and Numerical Weather Prediction (NWP) Research*, JMA, Japan, 188 pp. [Available at http://www.jma.go.jp/jma/jma-eng/jma-center/nwp/nwp-top.htm.

Japan Meteorological Agency, 2014: *JRA-55 product users' handbook: Model grid data.* JMA, Japan, 31 pp. [Available at http://jra.kishou.go.jp/JRA-55/index_en.html.]

Jones, P. D., D. H. Lister, T. J. Osborn, C. Harpham, M. Salmon, and C. P. Morice, 2012: Hemispheric and large-scale land surface air temperature variations: An extensive revision and an update to 2010. *J. Geophys. Res.*, **117**, D05127, doi:10.1029/2011JD017139.

Joseph, J. H., W. J. Wiscombe, and J. A. Weinman, 1976: The delta-Eddington approximation for radiative flux transfer. *J. Atmos. Sci.*, **33**, 2452–2459.

Juang, H.-M. H., 2004: A reduced spectral transform for the NCEP seasonal forecast global spectral atmospheric model. *Mon. Wea. Rev.*, **132**, 1019–1035.

Kalnay, E., M. Kanamitsu, R. Kistler, W. Collins, D. Deaven, L. Gandin, M. Iredell, S. Saha, G. White, J. Woollen, Y. Zhu, M. Chelliah, W. Ebisuzaki, W. Higgins, J. Janowiak, K. C. Mo, C. Ropelewski, J. Wang, A. Leetmaa, R. Reynolds, R. Jenne, and D. Joseph, 1996: The NCEP/NCAR 40-year reanalysis project. *Bull. Amer. Meteor. Soc.*, **77**, 437–471.

Kazumori, M., H. Owada, and K. Okamoto, 2004: Improvements of ATOVS radiance-bias correction scheme at JMA. *CAS/JSC WGNE Res. Activ. Atmos. Oceanic Modell.*, **34**, 15–16. [Available at http://www.wcrp-climate.org/WGNE/blue_book.html.]

Kistler, R., E. Kalnay, W. Collins, S. Saha, G. White, J. Woollen, M. Chelliah, W. Ebisuzaki, M. Kanamitsu, V. Kousky, H. van den Dool, R. Jenne, and M. Fiorino, 2001: The NCEP-NCAR 50-year reanalysis: Monthly means CD-ROM and documentation. *Bull. Amer. Meteor. Soc.*, **82**, 247–267.

Kitagawa, H., and S. Murai, 2006: A revised radiation scheme for cloud treatments in the Japan Meteorological Agency Global Spectral Model. *CAS/JSC WGNE Res. Activ. Atmos. Oceanic Modell.*, **36**, 17–18. [Available at http://www.wcrp-climate.org/WGNE/blue_book.html.]

Kitagawa, H., and S. Yabu, 2002: Impact of a revised parameterization of cloud radiative forcings on Earth's radiation budgets simulation. *CAS/JSC WGNE Res. Activ. Atmos. Oceanic Modell.*, **32**, section 4. [Available at http://www.wcrp-climate.org/WGNE/blue_book.html.]

Kobayashi, C., H. Endo, Y. Ota, S. Kobayashi, H. Onoda, Y. Harada, K. Onogi, and H. Kamahori, 2014: Preliminary results of the JRA-55C, an atmospheric reanalysis assimilating conventional observations only. *SOLA*, **10**, 78–82.

Kobayashi, C., and K. Shibata, 2011: Evaluation of dynamical contribution to lower stratospheric ozone trends in northern mid-latitudes over the last three decades (1980-2006) using a chemical transport model. *J. Meteor. Soc. Japan*, **89**, 363–376.

Kobayashi, S., M. Matricardi, D. Dee, and S. Uppala, 2009: Toward a consistent reanalysis of the upper stratosphere based on radiance measurements from SSU and AMSU-A. *Quart. J. Roy. Meteor. Soc.*, **135**, 2086–2099.

Kopp, G., G. Lawrence, and G. Rottman, 2005: The Total Irradiance Monitor (TIM): science results. *The Solar Radiation and Climate Experiment*. Springer., **230**, 129–139.

Kopp, G., and J. L. Lean, 2011: A new, lower value of total solar irradiance: evidence and climate significance. *Geophys. Res. Lett.*, **38**, L01706, doi:10.1029/2010GL045777.

Krzeminski, B., N. Bormann, G. Kelly, T. McNally, and P. Bauer, 2009: Revision of the HIRS cloud detection at ECMWF. *EUMETSAT/ECMWF Fellowship Programme Research Report*, **19**, ECMWF, UK, 15 pp. [Available at http://www.ecmwf.int/en/research/publications/.]

Liu, D. C., and J. Nocedal, 1989: On the limited memory BFGS method for large scale optimization. *Math. Programming*, **45**, 503–528.

Loeb, N. G., B. A. Wielicki, D. R. Doelling, G. L. Smith, D. F. Keyes, S. Kato, N. Manalo-Smith, and T. Wong, 2009: Toward optimal closure of the earth's top-of-atmosphere radiation budget. *J. Climate*, **22**, 748–766.

Maki, T., A. Ebita, T. Ishimizu, K. Nagata, M. Ikegami, and T. Sasaki, 2008: The daily 3D ozone produced by the chemical transport model for JRA-25. *Extended Abstracts of the Third WCRP International Conference on Reanalysis*, Tokyo, Japan. [Available at http://

wcrp.ipsl.jussieu.fr/Workshops/Reanalysis2008/abstract.html.]

Matricardi, M., F. Chevallier, G. Kelly, and J.-N. Thépaut, 2004: An improved general fast radiative transfer model for the assimilation of radiance observations. *Quart. J. Roy. Meteor. Soc.*, **130**, 153–173.

Matsumoto, T., M. Ishii, Y. Fukuda, and S. Hirahara, 2006: Sea ice data derived from microwave radiometer for climate monitoring. *Proceedings of the 14th Conference on Satellite Meteorology and Oceanography*, Atlanta, USA, 2.21–2.21.

McCarthy, M. P., H. A. Titchner, P. W. Thorne, S. F. B. Tett, L. Haimberger, and D. E. Parker, 2008: Assessing bias and uncertainty in the HadAT-adjusted radiosonde climate record. *J. Climate*, **21**, 817–832.

McMillin, L. M., D. Q. Wark, J. M. Siomkajlo, P. G. Abel, A. Werbowetzki, L. A. Pritchard, D. S. Crosby, H. M. Woolf, R. C. Luebbe, M. P. Weinreb, H. E. Fleming, F. E. Bittner, and C. M. Hayden, 1973: Satellite infrared soundings from NOAA spacecraft. *NOAA Technical Report NESS*, **65**, NOAA, USA, 112 pp.

Mears, C. A., and F. J. Wentz, 2009a: Construction of the Remote Sensing Systems V3.2 atmospheric temperature records from the MSU and AMSU microwave sounders. *J. Atmos. Oceanic Technol.*, **26**, 1040–1056.

Mears, C. A., and F. J. Wentz, 2009b: Construction of the RSS V3.2 lower tropospheric dataset from the MSU and AMSU microwave sounders. *J. Atmos. Oceanic Technol.*, **26**, 1493–1509.

Meinshausen, M., S. J. Smith, K. Calvin, J. S. Daniel, M. L. T. Kainuma, J.-F. Lamarque, K. Matsumoto, S. A. Montzka, S. C. B. Raper, K. Riahi, A. Thomson, G. J. M. Velders, and D. P. P. van Vuuren, 2011: The RCP greenhouse gas concentrations and their extensions from 1765 to 2300. *Climatic Change*, **109**, 213–241.

Nakagawa, M., 2009: Outline of the high resolution global model at the Japan Meteorological Agency. *RSMC Tokyo-Typhoon Center Technical Review*, **11**, JMA, Japan, 1–13. [Available at http://www.jma.go.jp/jma/jma-eng/jma-center/rsmc-hp-pub-eg/techrev.htm.]

Nakamura, H., T. Sampe, A. Goto, Q. Ohfuchi, and S.-P. Xie, 2008: On the importance of midlatitude oceanic frontal zones for the mean state and dominant variability in the tropospheric circulation. *Geophys. Res. Lett.*, **35**, L15709, doi:10.1029/2008GL034010.

Nash, J., 1988: Extension of explicit radiance observations by the stratospheric sounding unit into the lower stratosphere and lower mesosphere. *Quart. J. Roy. Meteor. Soc.*, **114**, 1153–1171.

Nash, J., and G. F. Forrester, 1986: Long-term monitoring of stratospheric temperature trends using radiance measurements obtained by the TIROS-N series of NOAA spacecraft. *Adv. Space Res.*, **6**, 37–44.

Nash, J., and R. Saunders, 2013: A review of stratospheric sounding unit radiance observations in support of climate trends investigations and reanalysis. *Forecasting Research Technical Report*, 586, Met Office, UK, 58 pp. [Available at http://www.metoffice.gov.uk/learning/library/publications/science/weather-science-technical-reports.]

NCDC, NWS, and FAA, 1981: *NCDC TD3200 U.S. cooperative summary of day, 1890(1948)-cont*. Research Data Archive at NCAR, Computational and Information Systems Laboratory, USA. [Available at http://rda.ucar.edu/datasets/ds510.0.]

Ohhashi, Y., 2004: Assimilation of QuikSCAT/SeaWinds ocean surface wind data into the JMA global data assimilation system. *RSMC Tokyo Typhoon Center Technical Review*, **7**, JMA, Japan, 22-27. [Available at http://www.jma.go.jp/jma/jma-eng/jma-center/rsmc-hp-pub-eg/techrev.htm.]

Okamoto, K., M. Kazumori, T. Egawa, T. Ishibashi, H. Owada, A. Murata, and H. Nishihata, 2011: Recent development of satellite data assimilation at JMA. *Proceedings of the Seventeenth International TOVS Study Conference*, Monterey, USA, 145–154. [Available at http://cimss.ssec.wisc.edu/itwg/itsc/.]

Okamoto, K., H. Owada, T. Egawa, and T. Ishibashi, 2008: Assimilation of radiance data at JMA: recent developments and prospective plans. *Proceedings of the Sixteenth International TOVS Study Conference*, Angra dos Reis, Brazil, 145–154. [Available at http://cimss.ssec.wisc.edu/itwg/itsc/.]

Okamoto, K., H. Owada, Y. Sato, and T. Ishibashi, 2007: Use of satellite radiances in the global assimilation system at JMA. *Proceedings of the Fifteenth International TOVS Study Conference*, Maratea, Italy, 162–171. [Available at http://cimss.ssec.wisc.edu/itwg/itsc/.]

Okamoto, N., M. D. Yamanaka, S.-Y. Ogino, H. Hashiguchi, N. Nishi, T. Sribimawati, and A. Numaguchi, 2003: Seasonal variations of tropospheric wind over Indonesia: comparison between collected operational radiosonde data and NCEP reanalysis for 1992–99. *J. Meteor. Soc. Japan*, **81**, 829–850.

Onogi, K., 1998: A data quality control method using forecasted horizontal gradient and tendency in a NWP system: Dynamic QC. *J. Meteor. Soc. Japan*, **76**, 497–516.

Onogi, K., 2000: *The long-term performance of the radiosonde observing system to be used for ERA-40.* ECMWF ERA-40 Project Report Series, 2. ECMWF, UK, 77 pp. [Available at http://www.ecmwf.int/en/research/publications/.]

Onogi, K., J. Tsutsui, H. Koide, M. Sakamoto, S. Kobayashi, H. Hatsushika, T. Matsumoto, N. Yamazaki, H. Kamahori, K. Takahashi, S. Kadokura, K. Wada, K. Kato, R. Oyama, T. Ose, N. Mannoji, and R. Taira, 2007: The JRA-25 reanalysis. *J. Meteor. Soc. Japan*, **85**, 369–432.

Ou, S.-C., and K.-N. Liou, 1995: Ice microphysics and climatic temperature feedback. *Atmos. Res.*, **35**,

127–138.

Parrish, D., and J. Derber, 1992: The National Meteorological Center's spectral statistical interpolation analysis system. *Mon. Wea. Rev.*, **120**, 1747−1763.

Raia, A., and I. F. A. Cavalcanti, 2008: The life cycle of the South American monsoon system. *J. Climate*, **21**, 6227–6246.

Räisänen, P., 1998: Effective longwave cloud fraction and maximum-random overlap of clouds: a problem and a solution. *Mon. Wea. Rev.*, **126**, 3336–3340.

Rienecker, M. M., M. J. Suarez, R. Gelaro, R. Todling, J. Bacmeister, E. Liu, M. G. Bosilovich, S. D. Schubert, L. Takacs, G.-K. Kim, S. Bloom, J. Chen, D. Collins, A. Conaty, A. da Silva, W. Gu, J. Joiner, R. D. Koster, R. Lucchesi, A. Molod, T. Owens, S. Pawson, P. Pegion, C. R. Redder, R. Reichle, F. R. Robertson, A. G. Ruddick, M. Sienkiewicz, and J. Woollen. 2011: MERRA: NASA's modern-era retrospective analysis for research and applications. *J. Climate*, **24**, 3624–3648.

Robel, J. (ed.), 2009: *NOAA KLM user's guide with NOAA-N, -N' supplement*. February 2009 revision, NOAA, USA. [Available at http://www.ncdc.noaa.gov/oa/pod-guide/ncdc/docs/klm/index.htm.]

Roberts, R. E., J. E. A. Selby, and L. M. Biberman, 1976: Infrared continuum absorption by atmospheric water vapor in the 8-12-μm window. *Appl. Opt.*, **15**, 2085–2090.

Rothman, L. S., A. Barbe, D. Chris Benner, L. R. Brown, C. Camy-Peyret, M. R. Carleer, K. Chance, C. Clerbaux, V. Dana, V. M. Devi, A. Fayt, J.-M. Flaud, R. R. Gamache, A. Goldman, D. Jacquemart, K. W. Jucks, W. J. Lafferty, J.-Y. Mandin, S. T. Massie, V. Nemtchinov, D. A. Newnham, A. Perrin, C. P. Rinsland, J. Schroeder, K. M. Smith, M. A. H. Smith, K. Tang, R. A. Toth, J. Vander Auwera, P. Varanasi, and K. Yoshino, 2003: The HITRAN molecular spectroscopic database: Edition of 2000 including updates through 2001. *J. Quant. Spectrosc. Radiat. Transfer*, **82**, 5–44.

Saha, S., S. Moorthi, H.-L., Pan, X. Wu, J. Wang, S. Nadiga, P. Tripp, R. Kistler, J. Woollen, D. Behringer, H. Liu, D. Stokes, R. Grumbine, G. Gayno, Y.-T. Hou, H.-Y. Chuang, H.-M. H. Juang, J. Sela, M. Iredell, R. Treadon, D. Kleist, P. van Delst, D. Keyser, J. Derber, M. Ek, J. Meng, H. Wei, R. Yang, S. Lord, H. van den Dool, A. Kumar, W. Wang, C. Long, M. Chelliah, Y. Xue, B. Huang, J.-K. Schemm, W. Ebisuzaki, R. Lin, P. Xie, M. Chen, S. Zhou, W. Higgins, C.-Z. Zou, Q. Liu, Y. Chen, Y. Han, L. Cucurull, R. W. Reynolds, G. Rutledge, and M. Goldberg, 2010: The NCEP climate forecast system reanalysis. *Bull. Amer. Meteor. Soc.*, **91**, 1015–1057.

Sakamoto, M., 2009: An update to the quality control thresholds of the conventional observing system for global data assimilation. *CAS/JSC WGNE Res. Activ. Atmos. Oceanic Modell.*, **39**, 33–34. [Available at http://www.wcrp-climate.org/WGNE/blue_book.html.]

Sakamoto, M., and J. Christy, 2009: The Influences of TOVS radiance assimilation on temperature and moisture tendencies in JRA-25 and ERA-40. *J. Atmos. Oceanic Technol.*, **26**, 1435–1455.

Sako, H., 2010: Assimilation of aircraft temperature data in the JMA global 4D-Var data assimilation system. *CAS/JSC WGNE Res. Activ. Atmos. Oceanic Modell.*, **40**, 33–34. [Available at http://www.wcrp-climate.org/WGNE/blue_book.html.]

Santer, B. D., T. M. L. Wigley, A. J. Simmons, P. W. Kållberg, G. A. Kelly, S. M. Uppala, C. Ammann, J. S. Boyle, W. Brüggemann, C. Doutriaux, M. Fiorino, C. Mears, G. A. Meehl, R. Sausen, K. E. Taylor, W. M. Washington, M. F. Wehner, and F. J. Wentz, 2004: Identification of anthropogenic climate change using a second-generation reanalysis. *J. Geophys. Res.*, **109**, D21104, doi:10.1029/2004JD005075.

Saunders, R., 2002: *RTTOV-7 science and validation report*. EUMETSAT NWP SAF, 51 pp. [Available at http://nwpsaf.eu/deliverables/rtm/.]

Saunders, R., 2008: *RTTOV-9 science and validation report*. EUMETSAT NWP SAF, 74 pp. [Available at http://nwpsaf.eu/deliverables/rtm/.]

Schneider, U., A. Becker, P. Finger, A. Meyer-Christoffer, B. Rudolf, and M. Ziese, 2011: GPCC full data reanalysis version 6.0 at 0.5°: monthly land-surface precipitation from rain-gauges built on GTS-based and historic data. doi:10.5676/DWD_GPCC/FD_M_V6_050. [Available at ftp://ftp.dwd.de/pub/data/gpcc/html/fulldata_v6_doi_download.html.]

Shibata, K., M. Deushi, T. T. Sekiyama, and H. Yoshimura, 2005: Development of an MRI chemical transport model for the study of stratospheric chemistry. *Pap. Geophys. Meteor.*, **55**, 75–119.

Shine, K. P., J. J. Barnett, and W. J. Randel, 2008: Temperature trends derived from stratospheric sounding unit radiances: The effect of increasing CO_2 on the weighting function. *Geophys. Res. Lett.*, **35**, L02710, doi:10.1029/2007GL032218.

Simmons, A. J., P. D. Jones, V. da Costa Bechtold, A. C. M. Beljaars, P. W. Kållberg, S. Saarinen, S. M. Uppala, P. Viterbo, and N. Wedi, 2004: Comparison of trends and low-frequency variability in CRU, ERA-40, and NCEP/NCAR analyses of surface air temperature. *J. Geophys. Res.*, **109**, D24115, doi:10.1029/2004JD005306.

Simmons, A. J., P. Poli, D. P. Dee, P. Berrisford, H. Hersbach, S. Kobayashi, and C. Peubey, 2014: Estimating low-frequency variability and trends in atmospheric temperature using ERA-Interim. *Quart. J. Roy. Meteor. Soc.*, **140**, 329–353.

Simmons, A. J., K. M. Willett, P. D. Jones, P. W. Thorne, and D. P. Dee, 2010: Low-frequency variations in surface atmospheric humidity, temperature, and

precipitation: Inferences from reanalyses and monthly gridded observational data sets. *J. Geophys. Res.*, **115**, D01110, doi:10.1029/2009JD012442.

Slingo, A., 1989: A GCM parameterization for the shortwave radiative properties of water clouds. *J. Atmos. Sci.*, **46**, 1419–1427.

Smith, S. J., and T. M. L. Wigley, 2006: Multi-gas forcing stabilization with Minicam. *Energy J.*, **27**, 373–391.

Takeuchi, Y., 2002: Algorithm theoretical basis document (ATBD) of the algorithm to derive total water vapor content from ADEOS-II/AMSR. *EORC Bull.*, **9**, 3–7. [Available at http://sharaku.eorc.jaxa.jp/AMSR/doc/index.html.]

Thompson, D. W. J., D. J. Seidel, W. J. Randel, C.-Z. Zou, A. H. Butler, C. Mears, A. Osso, C. Long, and R. Lin, 2012: The mystery of recent stratospheric temperature trends. *Nature*, **491**, 692–697.

Thorne, P. W., D. E. Parker, S. F. B. Tett, P. D. Jones, M. McCarthy, H. Coleman, and P. Brohan, 2005: Revisiting radiosonde upper-air temperatures from 1958 to 2002. *J. Geophys. Res.*, **110**, D18105, doi:10.1029/2004JD005753.

Trenberth, K. E., and J. T. Fasullo, 2010: Simulation of present-day and twenty-first-century energy budgets of the Southern Oceans. *J. Climate*, **23**, 440–454.

Trenberth, K. E., J. T. Fasullo, and J. Mackaro, 2011: Atmospheric moisture transports from ocean to land and global energy flows in reanalyses. *J. Climate*, **24**, 4907–4924.

Trenberth, K. E., and L. Smith, 2008: Atmospheric energy budgets in the Japanese reanalysis: Evaluation and variability. *J. Meteor. Soc. Japan*, **86**, 579–592.

Uppala, S. M., P. W. Kållberg, A. J. Simmons, U. Andrae, V. Da Costa Bechtold, M. Fiorino, J. K. Gibson, J. Haseler, A. Hernandez, G. A. Kelly, X. Li, K. Onogi, S. Saarinen, N. Sokka, R. P. Allan, E. Andersson, K. Arpe, M. A. Balmaseda, A. C. M. Beljaars, L. Van De Berg, J. Bidlot, N. Bormann, S. Caires, F. Chevallier, A. Dethof, M. Dragosavac, M. Fisher, M. Fuentes, S. Hagemann, E. Hólm, B. J. Hoskins, L. Isaksen, P. A. E. M. Janssen, R. Jenne, A. P. McNally, J.-F. Mahfouf, J.-J. Morcrette, N. A. Rayner, R. W. Saunders, P. Simon, A. Sterl, K. E. Trenberth, A. Untch, D. Vasiljevic, P. Viterbo, and J. Woollen, 2005: The ERA-40 re-analysis. *Quart. J. Roy. Meteor. Soc.*, **131**, 2961–3012.

van de Berg, L., J. Gustafsson, and A. Yildirim, 2002: Reprocessing of atmospheric motion vectors from Meteosat image data. *ECMWF ERA-40 Project Report Series*, 3, ECMWF, UK, 159–168. [Available at http://www.ecmwf.int/en/research/publications/.]

Veersé, F., D. Auroux, and M. Fisher, 2000: Limited-memory BFGS diagonal preconditioners for a data assimilation problem in meteorology. *Optimization and Engineering*, **1**, 323–339.

Walsh, J. E., and W. L. Chapman, 2001: 20th-century sea-ice variations from observational data. *Annals of Glaciology*, **33**, 444–448.

Wang, L., C.-Z. Zou, and H. Qian, 2012: Construction of stratospheric temperature data records from stratospheric sounding units. *J. Climate*, **25**, 2931–2946.

Werbowetzki, A. (ed.), 1981: *Atmospheric sounding user's guide.* NOAA Technical Report NESS, **83**, NOAA, USA, 82 pp.

Wild, M., D. Folini, C. Schär, N. Loeb, E. G. Dutton, and G. König-Langlo, 2013: The global energy balance from a surface perspective. *Climate Dyn.*, **40**, 3107–3134.

Wise, M., K. Calvin, A. Thomson, L. Clarke, B. Bond-Lamberty, R. Sands, S. J. Smith, A. Janetos, and J. Edmonds, 2009: Implications of limiting CO_2 concentrations for land use and energy. *Science*, **324**, 1183–1186.

WMO, 1986: *A preliminary cloudless standard atmosphere for radiation computation, World Climate Programme (WCP)*, **112**, 53 pp.

WMO, 2010: *Scientific Assessment of Ozone Depletion: 2010. Global Ozone Research and Monitoring Project.* **52**, WMO, Switzerland, 572 pp.

WMO, 2012: *WMO WDCGG data summary*. **36**, JMA, Japan, 100 pp. [Available at http://ds.data.jma.go.jp/gmd/wdcgg/products/publication.html.]

Wyser, K., 1998: The effective radius in ice clouds. *J. Climate*, **11**, 1793–1802.

Xie, S., and M. Zhang, 2000: Impact of the convection triggering function on single-column model simulations. *J. Geophys. Res.*, **105**, 14983–14996.

Yoshimura, H., and T. Matsumura 2003: A Semi-Lagrangian scheme conservative in the vertical direction. *CAS/JSC WGNE Res. Activ. Atmos. Oceanic Modell.*, **33**, 19–20. [Available at http://www.wcrp-climate.org/WGNE/blue_book.html.]

Zhong, W., and J. D. Haigh, 1995: Improved broadband emissivity parameterization for water vapor cooling rate calculations. *J. Atmos. Sci.*, **52**, 124–138.